The Astronomical Journal, 172:165 (21pp), 2026 September https://doi.org/10.3847/1538-3881/ae8770
© 2026. The Author(s). Published by the American Astronomical Society.
OPEN ACCESS

Biosignature Detectability on Transiting Habitable Worlds with the ELT/ANDES

Evann Kurzawa-Ferrandez[1], Aaron Bello-Arufe[1], and Renyu Hu[1,2,3,4]
[1] Jet Propulsion Laboratory, California Institute of Technology, Pasadena, CA 91109, USA; contact@evannkurzawa.com
[2] Department of Astronomy & Astrophysics, The Pennsylvania State University, University Park, PA 16802, USA
[3] Center for Exoplanets and Habitable Worlds, The Pennsylvania State University, University Park, PA 16802, USA
[4] Institute for Computational and Data Science, The Pennsylvania State University, University Park, PA 16802, USA
Received 2026 March 24; revised 2026 June 17; accepted 2026 July 1; published 2026 September 1

Abstract

The search for life beyond the solar system is at a turning point, transitioning from theoretical predictions to observations enabled by next-generation observatories. The Extremely Large Telescope (ELT) will host the Armazones High-dispersion Echelle Spectrograph (ANDES), optimized for visible to near-infrared high-resolution spectroscopy. We present a simulation–detection pipeline and evaluate the detectability of CO_2, H_2O, and the biosignature gases O_2 and CH_4 in high-resolution transmission spectroscopy of transiting habitable-zone rocky planets with ANDES. Assuming cloud-free, modern-Earth-like atmospheres, we model transmission spectra using noise estimates from the ANDES Exposure Time Calculator, based on the latest preliminary instrument design in seeing-limited mode. We introduce a novel Bayesian cross-correlation function (CCF) framework that incorporates molecule-specific kernels and a new autoregressive model to account for correlations in the CCF. We apply our framework to 18 known potentially habitable transiting exoplanets and estimate the number of transits required for a decisive detection ($\log_{10} B \geqslant 2.0$). We find that H_2O is the most accessible species, with potential detections in 10–19 transits for the TRAPPIST-1 planets and 30 transits for LHS 1140 b. CO_2, CH_4, and O_2 are more difficult to detect, requiring approximately 1.5, 3, and 4 times as many transits as H_2O, respectively. These estimates are lower limits that assume favorable observing conditions, perfect detrending, and the absence of systematics, yet still imply large observing campaigns. Alternative approaches, such as reflected-light high-dispersion coronagraphy of nearby nontransiting planets, may offer a promising complementary route for biosignature searches.

Unified Astronomy Thesaurus concepts: Bayesian statistics (1900); Exoplanet atmospheres (487); Ground telescopes (687); Habitable planets (695); High resolution spectroscopy (2096); Nested sampling (1894); Biosignatures (2018); Near infrared astronomy (1093); Transits (1711); Extrasolar rocky planets (511)

1. Introduction

With a 39 m diameter aperture, the Extremely Large Telescope (ELT) will be the largest optical and near-infrared (NIR) telescope in the world, equipped with a wide range of instruments. These include Armazones High-dispersion Echelle Spectrograph (ANDES; R. Maiolino et al. 2013; A. Marconi et al. 2022, 2024; V. D'Odorico et al. 2024; C. J. A. P. Martins et al. 2024; I. U. Roederer et al. 2024; E. Palle et al. 2025), a fiber-fed high-resolution spectrograph designed to provide $R \sim 100{,}000$ spectroscopy across the optical and NIR.

One of the main goals of ANDES is to search for potential biosignature gases in exoplanet atmospheres through high-resolution transmission spectroscopy (E. Palle et al. 2025). Among the gases potentially linked to planetary habitability, O_2, CO_2, CH_4, and H_2O are of primary importance. Specifically, CO_2 and H_2O govern greenhouse warming and water cycling for climate stability, while O_2 and CH_4 are short-lived and may signal active biological replenishment (S. Seager et al. 2012; V. S. Meadows et al. 2018; R. M. Ramirez 2018; E. W. Schwieterman et al. 2018; M. A. Thompson et al. 2022). Each of these four gases has distinct absorption features in the visible and/or NIR, making them prime candidates for searching for potentially habitable environments with ANDES. The instrument's high resolving power ($R \sim 100{,}000$), combined with the ELT's extremely large aperture, will provide unprecedented data quality for potentially habitable exoplanets (H. Kawahara et al. 2012; I. A. G. Snellen et al. 2013), far exceeding that of James Webb Space Telescope (JWST) spectroscopic modes ($R \sim 100$–3000; e.g., C. V. Morley et al. 2017; J. Lustig-Yaeger et al. 2019; D. Pidhorodetska et al. 2020).

Over the past decade, significant theoretical and observational advancements have been made, particularly in the use of high-resolution spectroscopy and transit observations to probe the atmospheres of rocky planets orbiting M dwarfs. Early studies, such as I. A. G. Snellen et al. (2013), proposed employing high-resolution spectroscopy ($R \sim 100{,}000$) and cross-correlation techniques to search for biosignature gases with extremely large telescopes such as the ELT. They estimated that detecting O_2 in the transmission spectrum of an Earth-analog orbiting an M5V star at 12 pc could be feasible after observing 30 transits. However, challenges such as the limited knowledge of the occurrence rate of habitable-zone Earth-sized planets around M dwarfs and the need to discover bright, nearby targets highlighted the difficulty of such endeavors.

F. Rodler & M. López-Morales (2014) revisited the estimates from I. A. G. Snellen et al. (2013) and found far less favorable results, with O_2 requiring up to 175 hr (~74 transits) to be detected on a target at 10 pc. The authors

Original content from this work may be used under the terms of the Creative Commons Attribution 4.0 licence. Any further distribution of this work must maintain attribution to the author(s) and the title of the work, journal citation and DOI.

concluded that nearby M4V stars are the most viable candidates, but even for these stars, achieving a significant detection remains challenging. D. B. Serindag & I. A. G. Snellen (2019) reinforced these findings by simulating O_2 detection in real observational data of Proxima Centauri, estimating the need for 20–50 transits for successful detection in optimal scenarios. Later, M. H. Currie et al. (2023) examined both inhabited and abiotic scenarios around M dwarfs and found that CO_2 and CH_4 are generally more accessible than O_2, which require substantially more observational effort, particularly for late-type host stars.

In parallel, large-scale surveys and theoretical simulations have advanced our understanding of the detectability of biosignature gases. K. K. Hardegree-Ullman et al. (2023) expanded on earlier work by creating a catalog of over 286,000 main-sequence stars within 120 pc and simulating a survey of M dwarfs within 20 pc. They concluded that detecting Earth-like O_2 levels within 50 yr is feasible for up to 21% of nearby M dwarf systems with suitable transiting planets, particularly if high-resolution spectrographs ($R \sim 500{,}000$) are utilized. They also noted that Earth-sized habitable-zone planets within 20 pc are far more numerous in nontransiting configurations than in transiting ones, highlighting the importance of observational techniques beyond the transit method. In response, several studies have explored the potential of direct imaging with next-generation ground-based observatories, focusing on nearby exoplanets. H. Zhang et al. (2024) demonstrated that instruments such as ELT/METIS and ELT/HARMONI could detect key atmospheric species, such as CH_4, CO_2, H_2O, and O_2, in nearby systems. Complementarily, K. K. Hardegree-Ullman et al. (2025) investigated the detectability of Earth-like O_2 levels in hypothetical habitable-zone exo-Earth candidates within 20 pc. Under optimistic assumptions and a 10 yr survey baseline, they found that O_2 at Earth-like abundances could be probed for up to ~7 and ~19 candidates using the Giant Magellan Telescope and ELT, respectively.

A complementary approach is to combine high-resolution spectroscopy with high-contrast imaging, often referred to as high-dispersion coronagraphy (HDC). In this technique, an adaptive-optics (AO) coronagraph spatially suppresses stellar light, and a high-resolution spectrograph disentangles the planet's Doppler-shifted molecular lines from the stellar spectrum (I. Snellen et al. 2015; D. Mawet et al. 2017; J. Wang et al. 2017). HDC is being developed on the ground (for example, with Keck/KPIC) and investigated for future space missions such as the Habitable Worlds Observatory (J. Wang et al. 2018; L. Pueyo et al. 2019; J. J. Wang et al. 2021). This approach may provide an alternative pathway for searching for biosignature gases in the reflected light of nearby habitable-zone planets. A major advantage of reflected-light HDC is that it does not require the planet to transit, thereby opening access to the nearest habitable worlds.

Although ground-based observations are affected by telluric contamination, they provide access to much larger collecting areas and spectral resolutions that remain unmatched by space telescopes. Two strategies for a comprehensive characterization of exoplanetary atmospheres are (i) combining ground- and space-based observations, as demonstrated by M. Brogi et al. (2017) and followed in other studies (e.g., D. Kasper et al. 2023; P. C. B. Smith et al. 2024), and (ii) increasing spectral resolution to facilitate the disentanglement of the planetary signal from the telluric and host-star spectra. M. López-Morales et al. (2019) demonstrated that raising the resolution from $R \sim 100{,}000$ to ~300,000–400,000 can double the depth of O_2 lines in Earth-like atmospheres, reducing the required number of transits by over 30%. Similarly, S. Rukdee (2024) showed that even under the most challenging haze and cloud conditions, increasing the resolution from $R \sim 100{,}000$ to ~300,000 enables robust detections with exposure times reduced by a factor of 4, thereby requiring significantly fewer transits.

ANDES represents the most advanced and promising ground-based instrument currently planned for the search for biosignature gases (E. Palle et al. 2025). Yet, a dedicated study of the number of transits that could be required to detect key atmospheric molecules on potentially habitable rocky exoplanets with ANDES has not yet been published. To address this gap, we present a framework that estimates transit requirements and target rankings under a homogeneous set of simplifying assumptions.

Our paper is structured as follows. In Section 2, we present the assumptions and models used to simulate the atmospheres of known transiting habitable-zone terrestrial planets. In Section 3, we generate the transmission spectra using the `petitRADTRANS` library (P. Mollière et al. 2019). Section 4 describes the ANDES observing setup, the Exposure Time Calculator (ETC)-based signal-to-noise ratio (S/N) estimates, and the noise injection procedure. In Section 5, we define the cross-correlation function (CCF) statistic adopted in this work and explain why a simple peak-based frequentist S/N estimate is not sufficiently robust for our sample. This motivates a more robust approach, introduced in Section 6, which details a custom Bayesian framework with `MultiNest` (F. Feroz et al. 2009), featuring interpolated kernels that mimic molecule-specific autocorrelation patterns and a first-order autoregressive (AR(1)) noise model that explicitly accounts for correlations between neighboring velocity bins in the CCF likelihood. Evidence estimation and Bayes factors are then used to quantify support for atmospheric-signal detection. In Section 7, we apply this framework to the planets and gases of interest. The results are then interpreted in Section 8, with emphasis on detectability, comparisons with prior work, and limitations of the adopted assumptions. Finally, in Section 9 we summarize the implications of these results for future ELT/ANDES observations.

2. Target Sample and Simulation Framework

The Habitable Worlds Catalog[5] (HWC; PHL @ UPR Arecibo 2026), last updated in 2024 March, identifies 70 potentially habitable worlds among the more than 5000 exoplanets known at that time.[6] Our analysis focuses on the 41 HWC planets with confirmed transits, out of a total of 70, and excludes 11 targets that are disfavored by our simplified ELT visibility screening, based on a sampled 20° altitude criterion (see Section 2.3). We further exclude 11 planets with radii larger than $2\,R_\oplus$, as planets above this threshold are unlikely to be rocky, and K2-288 B b, which falls within the radius valley, and whose lack of a measured mass means that this planet might not be rocky (B. J. Fulton et al. 2017).

[5] http://phl.upr.edu/hwc

[6] The NASA Exoplanet Archive (https://exoplanetarchive.ipac.caltech.edu/) currently lists over 6000 confirmed exoplanets.

2.1. Global Setup

The equilibrium temperature $T_{\rm eq}$ of each planet is estimated from blackbody theory, assuming a Bond albedo of 0.3 (e.g., G. Suissa et al. 2020; B. B. Siffert et al. 2024). Bulk planetary properties are listed in Table 1 and are taken from the NASA Exoplanet Archive (J. L. Christiansen et al. 2025). Planetary masses are estimated using the Bayesian radius–density–mass relation of H. Parviainen et al. (2024) via the `SPRIGHT` code. We use the maximum a posteriori estimate of the predicted mass distribution, which together with the radius defines the surface gravity g. The planetary reference radius $R_{\rm p}$ is defined at a reference pressure of 1 bar. The vertical grid spans pressures $\log_{10}(p/\mathrm{bar}) \in [-7, 0]$ using 100 layers, from 1 bar down to 10^{-7} bar ($\sim$120 km altitude for Earth-like conditions). In practice, we restrict radiative transfer to a single absorber at a time in order to isolate molecule-by-molecule accessibility within a simplified setup.

2.2. Atmospheric Model: Structure and Composition

1. *Temperature profile.* We adopt a two-layer temperature–pressure profile, a standard approximation in radiative–convective equilibrium models (e.g., J. F. Kasting et al. 1993; R. K. Kopparapu et al. 2013). The tropopause is set at 0.1 bar (T. D. Robinson & D. C. Catling 2014). Above this, the stratosphere is assumed to be isothermal at the atmospheric skin temperature, as described by, e.g., R. T. Pierrehumbert (2010) and V. Parmentier & T. Guillot (2014):

$$T_{\rm strat} = T_{\rm skin} \approx 2^{-1/4}\, T_{\rm eq}. \tag{1}$$

Below the tropopause, we assume a moist adiabatic temperature–pressure relation:

$$T(p) = T_{\rm skin}\left(\frac{p}{p_{\rm trop}}\right)^{\kappa_{\rm moist}}, \tag{2}$$

where $\kappa_{\rm moist} = 0.17$ approximates the lapse rate of a saturated Earth-like atmosphere and accounts for latent heat release during convection (T. D. Robinson & D. C. Catling 2012). This prescription ensures a continuous transition between the radiative and convective layers. The surface temperature is the moist adiabatic extension of $T_{\rm skin}$ to 1 bar.

2. *Atmospheric volume mixing ratios (VMRs).* The atmospheric composition is specified as follows.
   a. *H_2O.* For simplicity, we adopt an idealized two-level water vapor profile. The stratosphere is fixed to a constant VMR of 3 ppmv, representative of Earth's dry stratosphere (e.g., M. J. Prather 1989; L. Oman et al. 2008). In the troposphere, water vapor is assumed to be well mixed at a constant VMR of 0.3%, corresponding to a moderately humid Earth-like atmosphere. This value is not intended to reproduce the detailed vertical structure of terrestrial humidity, but is representative of the order of magnitude of Earth's tropospheric water vapor abundance (e.g., S. Heise et al. 2006; P. Gentine et al. 2013; P. Vergados et al. 2018).
   b. *O_3.* Described by a lognormal distribution in pressure as in P. von Paris et al. (2011, 2013), with peak mixing ratio of 10 ppmv centered at $p = 10$ mbar, width of $\sigma_{\ln p} = 0.5$, and a floor of 10 ppbv elsewhere (e.g., S. Bekki & F. Lefevre 2009; J. Kuttippurath et al. 2024).
   c. *CH_4.* Well mixed in the troposphere at 1.9 ppmv (X. Lan et al. 2025). Above the tropopause, the abundance is assumed to decrease exponentially with altitude, following A. E. Bainbridge & L. E. Heidt (1966); in pressure coordinates, we approximate this as $(p/p_{\rm trop})^{0.5}$.
   d. *CO.* We simplify the CO treatment of L. L. Pan et al. (2004) and L. El Amraoui et al. (2014) to a two-level profile: 100 ppbv in the troposphere and 50 ppbv in the stratosphere.
   e. *O_2.* Taken as a constant value of 0.2095 at all pressures, corresponding to the standard dry Earth atmosphere.
   f. *CO_2.* Taken as a constant value of 420 ppmv at all pressures (X. Lan et al. 2025).
   g. *N_2.* Fills the remaining fraction in each layer so that the total abundance sums to unity.

O_3, CO, and N_2 are included for completeness in the atmospheric composition, but are not included as opacity sources in the single-species runs. At each layer, all mixing ratios are renormalized to ensure $\sum_i x_i = 1$, and the mean molecular mass $\mu(p)$ is computed consistently.

The resulting vertical profiles of temperature and VMR are displayed in Figure 1.

2.3. Visibility Constraints and Planetary Velocity

The 2011 ELT construction proposal[7] specifies a minimum altitude cutoff of 20° (above the local horizon at the ELT site) to avoid rapid increases in atmospheric extinction, dome vignetting, and seeing degradation that arise at lower altitudes. In this work, we use this limit as a simplified visibility criterion to exclude targets that are strongly disfavored from the ELT site.

To construct a coarse annual visibility metric for each host star, we generate a uniform grid of 366 epochs spanning 2025 January 1–2026 January 1, and transform its coordinates from the International Celestial Reference System to the ELT altitude–azimuth frame using `Astropy` (Astropy Collaboration 2022). At each sampled epoch, we evaluate the apparent altitude of the star and identify the epochs for which the altitude exceeds 20°. Consequently, we retain only planets whose host stars satisfy the adopted 20° altitude criterion at least once within the sampled annual grid and exclude those for which no such sampled epoch exists. This cut therefore provides a consistent first-order visibility criterion for defining the target sample, while more detailed scheduling effects are left to future observation-specific planning.

In parallel, we compute the barycentric velocity correction at each sampled epoch using a DE430 ephemeris and the `barycorrpy` package (S. Kanodia & J. Wright 2018), following the algorithm of J. T. Wright & J. D. Eastman (2014). For each retained target, this yields an annual time series of barycentric corrections over the subset of sampled epochs that satisfy the altitude cut. An example is shown in Figure 2.

[7] https://www.eso.org/public/products/books/book_0046/

Table 1
Input Parameters for `petitRADTRANS` and the ETC

Planet	a (au)	d_* (pc)	P (days)	T_{14} (hr)	T_{eq} (K)	R_p ($R_\oplus$)	R_* ($R_\odot$)	M_p ($M_\oplus$)	T_* (K)	v_{sys} (km s^{-1})	v_{bary} (km s^{-1})	Sp. T.	m_J (Vega)	References
K2-3 d	0.210	44.07	44.556	4.170	286†	1.620	0.600	5.217†	3835	30.24	29.39†	M0V	9.42	1, 2, 3, 4, 5
K2-72 e	0.106	66.43	24.159	2.250	272†	1.290	0.329	2.211†	3498	−42.92	0.69†	M2V	11.69	1, 2, 6, 7, 8
Kepler-1649 c	0.083	92.19	19.535	1.070	239†	1.060	0.232	1.101†	3240	0.00†	−13.61†	M5V	13.38	1, 9, 10
Kepler-186 f	0.432	177.59	129.943	5.448	193†	1.438	0.548	3.306†	3876	−60.96	−7.58†	M1	12.47	1, 2, 7, 11, 12, 13, 14, 15
Kepler-440 b	0.242	301.03	101.111	8.130	284†	1.899	0.663	4.140†	3891	−20.61	−7.23†	K8V†	12.96	1, 2, 7, 11, 12, 13, 14
Kepler-442 b	0.409	365.97	112.303	5.630	248†	1.395	0.619	2.958†	4563	−76.91	−6.72†	K4V†	13.23	1, 2, 7, 11, 12, 13, 14
Kepler-452 b	1.046	551.73	384.843	10.367	261†	1.511	1.119	3.983†	5728	−25.49	−7.80†	G2	12.26	1, 2, 7, 13, 14, 16
Kepler-62 e	0.428	300.87	122.386	7.196	279†	1.873	0.731	3.971†	4842	17.51	−9.65†	K2V	12.26	1, 2, 7, 13, 17, 18
Kepler-62 f	0.720	300.87	267.283	7.460	215†	1.540	0.731	4.291†	4842	17.51	−9.65†	K2V	12.26	1, 2, 7, 17, 18, 19
LHS 1140 b	0.095	14.99	24.737	2.150	206†	1.730	0.216	6.764†	3096	−13.74	−28.80†	M4.5V	9.61	1, 2, 20
LP 890-9 c	0.040	32.43	8.457	0.959	248†	1.367	0.156	2.740†	2850	28.84	19.99†	M6V	12.26	1, 2, 21
TOI-700 d	0.163	31.13	37.424	3.314	245†	1.073	0.421	1.146†	3459	−4.78	1.78†	M2.5V	9.47	1, 22, 23
TOI-700 e	0.134	31.13	27.810	2.777	270†	0.953	0.421	0.757†	3459	−4.78	1.78†	M2.5V	9.47	1, 22, 23
TOI-715 b	0.083	42.40	19.288	1.980	231†	1.550	0.240	4.395†	3075	55.78	−4.49†	M4	11.81	1, 2, 24
TRAPPIST-1 d	0.022	12.43	4.049	0.815	263†	0.788	0.119	0.394†	2566	−52.00	0.22†	M8V	11.35	1, 25, 26, 27, 28
TRAPPIST-1 e	0.029	12.43	6.101	0.929	229†	0.920	0.119	0.671†	2566	−52.00	0.22†	M8V	11.35	1, 25, 26, 27, 28
TRAPPIST-1 f	0.038	12.43	9.208	1.048	200†	1.045	0.119	1.044†	2566	−52.00	0.22†	M8V	11.35	1, 25, 26, 27, 28
TRAPPIST-1 g	0.047	12.43	12.352	1.137	180†	1.129	0.119	1.373†	2566	−52.00	0.22†	M8V	11.35	1, 25, 26, 27, 28

Notes. Here, a is the semimajor axis; d_* is the distance to the star; P is the orbital period; T_{14} is the transit duration; T_{eq} is the planetary equilibrium temperature; R_p is the planet radius; R_* is the host-star radius; M_p is the planet mass; T_* is the host-star effective temperature; v_{sys} is the host-star systemic velocity; v_{bary} is the barycentric correction that maximizes $|v_{sys} - v_{bary}|$ over the course of a year; Sp. T. is the host-star spectral type; and m_J is the Vega magnitude of the host star in the J band. When v_{sys} is unavailable, a default value of 0 km s^{-1} is assumed as a simplifying approximation. Values marked with a dagger (†) were calculated in this work. These data are obtained in part from the SIMBAD database and the NASA Exoplanet Archive.

References: (1) Two Micron All Sky Survey catalog; R. Cutri et al. (2003); (2) Gaia Collaboration (2023); (3) A. Fukui et al. (2016); (4) A. S. Bonomo et al. (2023); (5) H. Diamond-Lowe et al. (2022); (6) C. D. Dressing et al. (2017); (7) TESS Input Catalog: K. G. Stassun et al. (2019); (8) I. J. M. Crossfield et al. (2016); (9) A. Vanderburg et al. (2020); (10) K. K. Hardegree-Ullman et al. (2019); (11) G. Torres et al. (2015); (12) P. Gajdoš et al. (2019); (13) T. D. Morton et al. (2016); (14) T. A. Berger et al. (2018); (15) E. V. Quintana et al. (2014); (16) J. M. Jenkins et al. (2015); (17) L. M. Weiss et al. (2024); (18) W. J. Borucki et al. (2013); (19) W. Borucki et al. (2018); (20) C. Cadieux et al. (2024a); (21) L. Delrez et al. (2022); (22) E. A. Gilbert et al. (2023); (23) Abdurro'uf et al. (2022); (24) G. Dransfield et al. (2024); (25) E. Agol et al. (2021); (26) H. Jönsson et al. (2020); (27) J. E. Gizis et al. (2000); (28) C. Piaulet-Ghorayeb et al. (2025).

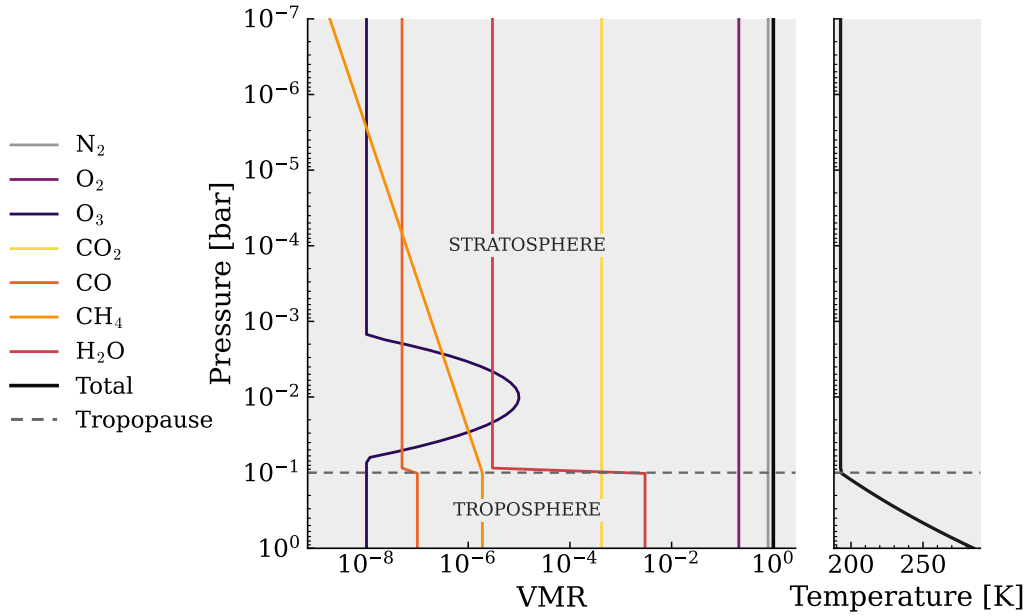


Figure 1. Vertical profiles of temperature and VMRs for the species included in our atmospheric model, simulated for TRAPPIST-1 e. The profile behavior follows from the equations and assumptions described in Section 2.2.

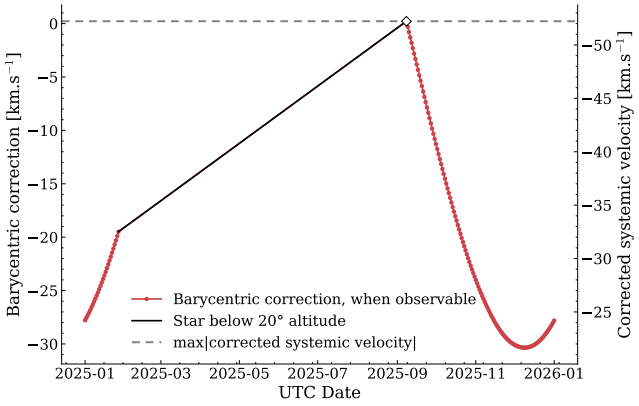


Figure 2. Barycentric velocity correction for TRAPPIST-1 from 2025 January to 2026 January. In our screening framework, sampled epochs between February and September do not satisfy the adopted 20° criterion. Over the retained epochs, the barycentric correction varies between approximately −30 and 0 km s^{-1}. The sinusoidal modulation reflects the projection of Earth's nearly circular orbital velocity onto the line of sight to the star, producing a radial component with an amplitude of about ±30 km s^{-1} and a 1 yr period, phase shifted according to the star's ecliptic position. The right-hand y-axis shows the relative Doppler separation $v_{\rm sys} - v_{\rm bary}(t)$, whose absolute value is maximized for TRAPPIST-1 at a barycentric velocity of 0.22 km s^{-1} within this framework.

Among the sampled epochs that satisfy the screening criterion, we adopt the most optimistic Doppler-separation configuration by selecting the epoch at which the absolute difference between the systemic velocity and the barycentric correction is largest:

$$v_{\rm max} = v_{\rm sys} - v_{\rm bary}(t_{\rm max}),$$
$$t_{\rm max} = \arg\max_t |v_{\rm sys} - v_{\rm bary}(t)|. \quad (3)$$

We use this quantity as a best-case proxy for the barycentric-systemic offset in the synthetic observations. The systemic velocities and the corresponding sampled barycentric corrections at maximum separation are summarized in Table 1.

3. Building Exoplanet Transmission Spectra

We generate model transmission spectra with `petitRADTRANS` (P. Mollière et al. 2019), which performs radiative transfer for planetary atmospheres. For each target, we use published HWC system parameters together with our atmospheric model as inputs.

In all simulations, we include Rayleigh scattering by N_2; clouds are not modeled. We also neglect atmospheric refraction under the conditions relevant to our targets (temperate, warm, close-in rocky planets around K–M dwarfs). In this regime, the large stellar angular size pushes the refractive boundary to pressures and altitudes where gas and Rayleigh opacity dominate the slant optical depth, so refraction makes only a minor contribution and does not set the continuum for our targets. This behavior is captured by analytic refractive-boundary estimates and validated against ray-tracing comparisons (T. D. Robinson et al. 2017); for the Earth–Sun case, refraction excludes only the lowest ∼13 km and changes the effective radius by at most a few tens of kilometers across the optical–NIR (Y. Bétrémieux & L. Kaltenegger 2013).

Because our analysis relies on high-resolution spectroscopy, we adopt molecular opacity data at commensurate resolution. For H_2O, CO_2, and CO, we use the HITEMP line lists (L. S. Rothman et al. 2010); for CH_4 we use the HITEMP update by R. J. Hargreaves et al. (2020); for O_3, the HITRAN database (L. S. Rothman et al. 2013); for O_2, the HITRAN compilation (I. E. Gordon et al. 2022); and for N_2, the WCCRMT database (C. M. Western et al. 2018). The H_2O, CO_2, CO, O_3, and CH_4 opacity files are obtained in HDF5 format from the Keeper knowledge base of the Max Planck Digital Library,[8] while those for O_2 and N_2 are binary files from the DACE Opacity Database,[9] which employs the open-source `HELIOS-K` code (S. L. Grimm & K. Heng 2015; S. L. Grimm et al. 2021) to convert line lists into opacity

[8] https://keeper.mpdl.mpg.de/
[9] https://dace.unige.ch

coefficients suitable for atmospheric simulations. Each binary file corresponds to a specific temperature, pressure, and wavenumber range, which we merge into a single line-by-line file readable by `petitRADTRANS`.

We simulate a time series of spectra spanning twice the transit duration and centered on midtransit. Prior to resampling, we apply instrumental broadening by convolving each spectrum with a Gaussian kernel whose width is set by the ANDES resolving power. The convolution is performed using the `PyAstronomy` library (S. Czesla et al. 2019). We choose to extend the Gaussian kernel to five standard deviations to ensure computational efficiency while adequately representing the instrument response. After broadening, we convert vacuum wavelengths to air wavelengths using the B. Edlén (1966) relation. The broadened spectra are then interpolated onto a constant-R wavelength grid (described in Section 4.2). We neglect other contributions to the broadening or Doppler shifting of the planet spectrum (e.g., planetary rotation and atmospheric dynamics), consistent with the deliberately simplified scope adopted here.

The stellar spectrum used in the synthetic observations is based on the stellar count spectrum returned by the ANDES ETC, as described in Section 4. We Doppler shift the stellar spectrum by $v_{\rm max}$ and the planet's transmission spectrum by

$$v_{\rm tot}(t) = v_{\rm p}(t) + v_{\rm max}, \tag{4}$$

where $v_{\rm tot}(t)$ is the planet–ELT line-of-sight velocity during transit, $v_{\rm p}(t)$ is the planet's radial velocity in the star–planet frame, and $v_{\rm max}$ is the constant barycentric-systemic offset at the epoch of maximum Doppler separation (Equation (3)). The planet's radial velocity is given by

$$v_{\rm p}(t) = K_{\rm p} \sin(2\pi\phi(t)), \tag{5}$$

where $\phi(t)$ is the orbital phase at time t and $K_{\rm p}$ is the radial-velocity semiamplitude of the planet:

$$K_{\rm p} = \frac{2\pi a \sin(i_{\rm p})}{P\sqrt{1-e^2}}, \tag{6}$$

where a is the orbital semimajor axis of the planet, $i_{\rm p}$ is the orbital inclination, P is the orbital period, and e is the eccentricity. We assume circular orbits in our simulations.

We then inject the Doppler-shifted planetary transmission spectrum during the in-transit window. The observed spectrum model is

$$S_{\rm obs}(\lambda) = S_{\rm star}(\lambda) \times (1 - S_{\rm planet}), \tag{7}$$

where $S_{\rm star}$ is the ETC-derived stellar count spectrum Doppler shifted by $v_{\rm max}$ (Equation (3)), and $S_{\rm planet}$ is the transit depth shifted by $v_{\rm tot}$ (Equation (4)) and set to zero outside of transit. $S_{\rm obs}$ is the composite planet–host star spectrum.

4. Synthetic Observations with ELT/ANDES

4.1. Observing Mode

After generating the spectral models, we add noise consistent with the expected performance of ANDES. The instrumental assumptions adopted here are based on the ANDES design available during the review of this paper in 2026 June. Because the design is still evolving ahead of the Preliminary Design Review, these assumptions should be regarded as current best estimates. The instrument is a fiber-fed, high-resolution spectrograph for the ELT with several observing modes. The configuration relevant for this work is the seeing-limited point-source mode, which provides $R \sim 100{,}000$ spectroscopy over the broad optical–NIR wavelength range used here, with separate object and sky apertures. ANDES also includes an AO-assisted integral-field-unit (IFU) mode in the NIR, designed for diffraction-limited observations and high-contrast, reflected-light applications. This IFU mode can use up to 61 spatial elements, or spaxels, with selectable spaxel scales in the 5–100 mas range (A. Marconi et al. 2024; E. Palle et al. 2025). However, our simulations concern unresolved transmission spectroscopy of transiting planets, for which the star and planet are observed together as a point source. We therefore use the seeing-limited mode, not the AO-assisted IFU mode, and the relevant spatial factor in the detector-noise term is the effective number of detector pixels in the seeing-limited extraction aperture.

4.2. Signal-to-noise Ratio Grid

4.2.1. ETC Signal-to-noise Ratio Scale

S/Ns under our observing conditions are obtained from the ANDES ETC[10] (N. Sanna et al. 2014, 2021, 2024). We use the latest ETC release available at the time of revision, v.5.2,[11] to set the absolute S/N scale. The exported v.5.2 wavelength points, however, are representative S/N samples and do not form a fully sampled high-resolution grid. To recover the dense wavelength sampling needed for the spectral simulations, we also use ETC v.3.2,[12] which returns a densely sampled S/N curve, including small-scale variations caused by telluric absorption and instrumental response. We therefore rescale the dense v.3.2 S/N curve locally to match the v.5.2 S/N anchors. Both ETC outputs are first evaluated for a 600 s reference exposure (see Section 4.3).

We denote by $\lambda_i^{\rm v.3.2}$ and $({\rm S/N})_{\rm v.3.2}(\lambda_i^{\rm v.3.2})$ the dense wavelength grid and S/N values from v.3.2. We denote by $\lambda_j^{\rm v.5.2}$, $({\rm S/N})_{\rm v.5.2}(\lambda_j^{\rm v.5.2})$, and $N_{\star,{\rm v.5.2}}(\lambda_j^{\rm v.5.2})$ the v.5.2 wavelength points, S/N values, and detected stellar signal for the same exposure time, respectively. $N_{\star,{\rm v.5.2}}$ corresponds to the ETC "object" signal from the host star, expressed in e^- per resolution element.

At each v.5.2 wavelength point, we interpolate the v.3.2 S/N onto $\lambda_j^{\rm v.5.2}$ and compute the local scale factor

$$f_j = \frac{({\rm S/N})_{\rm v.5.2}(\lambda_j^{\rm v.5.2})}{({\rm S/N})_{\rm v.3.2}(\lambda_j^{\rm v.5.2})}. \tag{8}$$

Each v.5.2 wavelength point defines a bin centered on that point, with edges halfway to the adjacent v.5.2 points. For a v.5.2 wavelength point $\lambda_j^{\rm v.5.2}$, the bin boundaries are

$$\lambda_{j\pm1/2}^{\rm v.5.2} = \frac{1}{2}\left(\lambda_j^{\rm v.5.2} + \lambda_{j\pm1}^{\rm v.5.2}\right). \tag{9}$$

Within the interval associated with $\lambda_j^{\rm v.5.2}$, we multiply the dense v.3.2 S/N by the corresponding factor f_j:

$$({\rm S/N})_{\rm ETC}(\lambda) = f_j\,({\rm S/N})_{\rm v.3.2}(\lambda), \quad \lambda_{j-1/2}^{\rm v.5.2} \leqslant \lambda < \lambda_{j+1/2}^{\rm v.5.2}. \tag{10}$$

[10] https://andes.inaf.it/instrument/exposure-time-calculator/
[11] Release: 2026 April 17, https://andes-etc.brera.inaf.it/.
[12] Release: 2024 September 9.

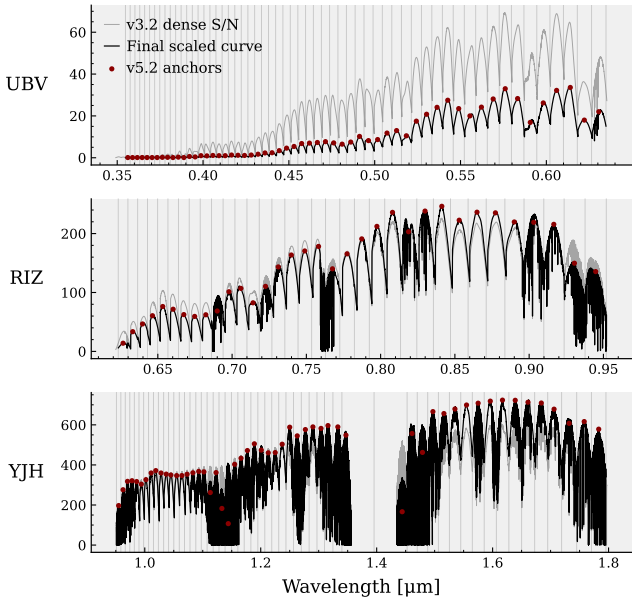


Figure 3. Construction of the ETC S/N curve, shown here for TRAPPIST-1 and a 600 s reference exposure. The red points show the representative S/N anchors from v.5.2, which set the absolute normalization. The gray curves show the densely sampled wavelength structure from v.3.2. For each v.5.2 anchor, we compute a local multiplicative scale factor (Equation (8)) and apply it to the corresponding v.3.2 wavelength interval. The resulting scaled S/N curve is shown in black. Thin vertical lines indicate the wavelength intervals assigned to each v.5.2 anchor point.

This produces an ETC S/N curve that follows the v.5.2 normalization locally while retaining the dense wavelength structure available from v.3.2. This construction is illustrated in Figure 3.

4.2.2. Constant-resolution Grid

After defining the S/N scale, we place the simulated spectra, S/N values, and stellar count spectrum on a common wavelength grid with one point per resolution element. This ensures that the model spectra are sampled at the same resolution-element scale at which the ETC reports the S/N and detected stellar signal, and at which the instrumental broadening is defined. The corresponding constant-R sampling is defined by

$$\Delta \ln \lambda = \frac{1}{R}, \tag{11}$$

or, equivalently

$$\lambda_{k+1} = \lambda_k \exp\left(\frac{1}{R}\right). \tag{12}$$

This grid is uniform in resolving power, $\Delta\lambda/\lambda \simeq 1/R$, and therefore provides one sample per resolution element over the wavelength range retained from the ETC output. The S/N curve from Equation (10) is interpolated onto this constant-R grid. The v.5.2 stellar count spectrum is interpolated onto the same grid and used as the stellar spectrum in the observation model.

4.3. Assumptions and Inputs to the ETC

Table 2 summarizes the main instrumental and observing parameters used in the ETC calculations. We assume an airmass of 1.0 and adopt an integration time of 10 minutes per exposure. This choice is short enough to avoid significant orbital smearing of the planetary absorption lines during individual exposures; using the orbital parameters in Table 1, we estimate the maximum line-of-sight velocity drift over a 10 minute exposure at midtransit, where the velocity changes most rapidly; the largest drift in our sample occurs for TRAPPIST-1 d, with $\Delta v_{\rm exp} \simeq 0.64\,{\rm km\,s^{-1}}$. This is smaller than the ANDES pixel scale of approximately $1.0\,{\rm km\,s^{-1}}$, assuming $R \simeq 100{,}000$ and 3 pixels per resolution element. Therefore, the planetary lines remain within the same spectral pixel during an exposure, and orbital smearing is negligible for all targets in our sample. A target-by-target optimization of the exposure time, including readout overheads and detector systematics, is beyond the scope of this work. For each target, we provide the host star's J-band Vega magnitude and spectral type, as listed in Table 1. Because the ETC relies on a finite set of models from the A. J. Pickles (1998) stellar library, we approximate each true spectral type by the closest available option.

Table 2
Main ANDES ETC Parameters

Quantity	Adopted Value or Treatment
Observing mode	Seeing-limited point-source mode
Resolving power	100,000
Exposure time (s)	600
Airmass	1.0
Magnitude	J-band Vega system (see Table 1)
Stellar templates	Closest available A. J. Pickles (1998)-library spectral type
Seeing (arcsec)	0.8
Sky transparency	Photometric
Moon phase	0
Binning	1×1
Number of separate readouts	1

Note. Parameters used for the ETC v.5.2 calculations. ANDES includes an AO-assisted IFU, but the present transmission-spectroscopy simulations use the seeing-limited point-source mode.

Although readout noise is included in our calculations, we ignore the readout overhead; for the several-minute exposures considered here, the per-frame overhead is expected to be small (a few percent at most), so this approximation does not materially affect our results.

The sky-background term is taken directly from the wavelength- and airmass-dependent sky-background tables distributed with the ANDES ETC, separately for the *UBV*, *RIZ*, and *YJH* bands. The ETC tables used here do not expose separate OH-airglow, zodiacal-light, moonlight, or optical-sky components, so we cannot decompose the sky-background term into individual physical contributions. We therefore use the total ETC sky-background model directly.

To evaluate whether an additional OH-line mask would substantially reduce the usable wavelength range, we estimate the fractional coverage of OH-line cores using the ESO SOFI OH-line list.[13] We mask $\pm 2\lambda/R$ around each tabulated line at $R = 100{,}000$, merge overlapping intervals, sum the resulting OH-covered wavelength intervals, and divide by the total

[13] https://www.eso.org/sci/facilities/lasilla/instruments/sofi/tools/OHskyLines.html

wavelength span. This gives an OH-core coverage of only $\simeq$1.1% over the NIR wavelength range covered by the ETC output, with approximate *Y*, *J*, and *H* fractions of 1.0%, 1.7%, and 2.0%, respectively. This is not a full OH-emission model, but it shows that the loss of wavelength coverage would be small at ANDES resolution.

4.4. Building the Final Spectra

Using the procedure described in Section 4.2, we obtain three arrays for each band on the same reconstructed constant-*R* wavelength grid: the wavelength array, the ETC S/N per resolution element, and the v.5.2 stellar count spectrum. The band-specific arrays are concatenated to form a single spectrum and the effective exposure time is derived based on the assumed 10 minute integration time.

The ETC includes telluric absorption through a TAPAS-based atmospheric-transmission spectrum (J. L. Bertaux et al. 2014). Thus, the wavelength dependence of the ETC-derived throughput and S/N already reflects atmospheric-transmission losses. In our simulations, we do not apply an additional multiplicative telluric spectrum to the synthetic planet–star spectra. We instead assume that telluric lines can be corrected down to the photon-noise level, with the most affected regions removed by the S/N masks described below; the limitations of this optimistic assumption are discussed in Section 8.4.

We then apply a two-step S/N mask before adding synthetic noise. First, we discard the lowest-S/N 3% of ETC wavelength elements over the full wavelength range. This global cut was chosen empirically to remove the strongest low-S/N outliers in the ETC wavelength grid while preserving nearly all of the usable spectral coverage. A comparison with TAPAS atmospheric-transmission models shows that these rejected pixels are strongly enriched in telluric absorption regions; across the planets tested, the median fraction of rejected pixels with TAPAS transmission below 0.8 is 37.0%, compared with 1.7% among retained pixels. The rejected pixels are therefore not selected from a predefined telluric or OH-line mask; they also include wavelengths at the edges of the instrumental range where the predicted S/N drops. We then divide the spectrum into 0.06 μm bins and, within each bin, discard the lowest 5% of ETC wavelength elements by S/N, as well as any pixels with zero S/N. We then intersect these masks across all transit counts, retaining only pixels that satisfy the S/N threshold for every exposure. This ensures that all exposure times share an identical wavelength grid. We then add synthetic Gaussian noise on the retained wavelength grid using the corresponding ETC S/N values.

We normalize each simulated spectrum by sequentially dividing it by its out-of-transit time-averaged stellar baseline, and its median spectrum along wavelength to correct for throughput variations and stellar continuum fluctuations. The corresponding uncertainty from the finite out-of-transit baseline is propagated analytically, including covariance terms for out-of-transit exposures. The noisy spectrum is also continuum normalized as described by A. Bello-Arufe et al. (2023). To do so, we first fit the continuum using a Gaussian filter with a standard deviation of $\sim$500 pixels. We then divide the spectrum by the continuum such that we isolate high-frequency spectral features while suppressing the low-frequency continuum. We propagate the pixel uncertainties accordingly. This spectrum is then used as input for a cross-correlation analysis to evaluate the detection significance as a function of the number of observed transits. For clarity, the complete procedure for constructing this final spectrum is summarized in Figure 4.

5. Cross-correlation Function Analysis and Limitations of Peak Signal-to-noise Ratio Estimates

Having generated the noisy spectra, we next define the cross-correlation statistic used throughout this work. For each planet–molecule configuration, Monte Carlo realization, and assumed cumulative number of transits *n*, we simulate a phase-sampled sequence spanning twice the transit duration and centered on midtransit (Section 4).

For the final detection step, we reduce each normalized sequence to a single representative central in-transit exposure and compute a one-dimensional CCF from that spectrum. The time series still enters the analysis through the construction of the out-of-transit reference spectrum and the propagated uncertainty budget. We adopt this choice as a simple and homogeneous approach across the large grid of planet–molecule configurations explored here. In particular, it avoids introducing additional assumptions about how to combine spectra obtained at different in-transit velocities and phases, and it places all targets on the same footing when comparing relative detectability. The CCF is therefore well suited to the comparative objectives of this study, although a phase-resolved combination of all in-transit spectra may affect the absolute detection strengths.

For each cumulative transit count *n*, we cross correlate the baseline-corrected, continuum-normalized representative in-transit spectrum, $S_{\rm obs}(\lambda,\ n)$, with a noiseless molecular template, $S_T(\lambda,\ v)$, shifted from -200 to 200 km s^{-1} in steps of 1 km s^{-1}. To ensure a common wavelength interval for all trial velocities, we truncate the spectrum to the subset of pixels that remain valid after Doppler shifting over the full velocity range. For each trial velocity, the shifted template is normalized to unit sum and mean subtracted over the retained wavelength interval; the observed spectrum is mean subtracted over that same interval. The CCF is inverse-variance weighted, using the per-pixel variances propagated through the out-of-transit, continuum, and median normalizations. Using the propagated variance $\sigma^2(\lambda,\ n)$, we compute

$$c(v,\ n) = \sum_{\lambda} \frac{\left[S_T(\lambda,\ v) - \bar{S_T}(v)\right]\left[S_{\rm obs}(\lambda,\ n) - \bar{S_{\rm obs}}(n)\right]}{\sigma^2(\lambda,\ n)}, \tag{13}$$

where the overbars denote the mean over the retained wavelength interval.

In the CCF, the planetary contribution is expected near the known reference velocity $v_{\rm tot}$ (Equation (4)). A common approach in the literature is to estimate a detection significance by dividing the CCF peak amplitude by the standard deviation of CCF values far from the expected planetary signal (e.g., M. Brogi et al. 2013; R. J. de Kok et al. 2013; A. Bello-Arufe et al. 2022). In our simulations, however, this approach is not sufficiently robust. Although we assume ideal telluric correction at the spectral level, wavelengths coincident with strong telluric absorption have lower S/N in the ETC output and therefore contribute noisier pixels to the CCF. Because these wavelengths are fixed in the observer frame, their contribution tends to produce enhanced variance, and occasionally localized positive or negative peaks, near $v = 0$ km s^{-1} in

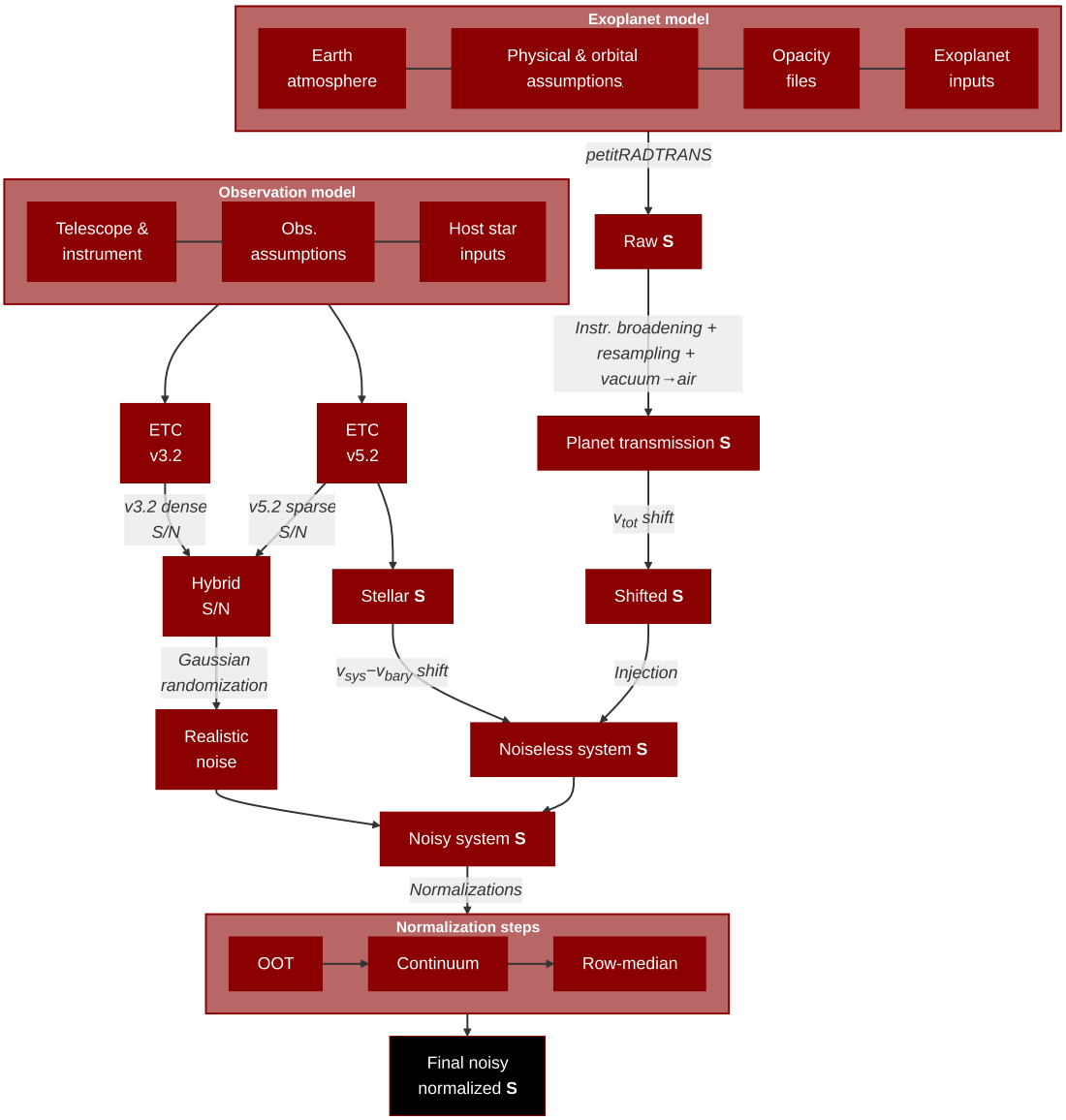


Figure 4. Workflow for constructing the high-resolution transmission spectrum used as input to the CCF analysis for a given molecule–planet pair. Here, ***S*** denotes the spectrum at each stage of the workflow.

the CCF. These features must be interpreted as noise associated with telluric absorption bands, and are not an explicitly simulated residual telluric spectrum. The CCF baseline is also not flat, the variance changes with velocity, and neighboring velocity bins are correlated because nearby shifted templates overlap strongly in wavelength space. As a result, the far-from-peak standard deviation is not a reliable local noise estimate, and peak-based S/N values can lead to biased target rankings.

As a first mitigation, we apply the wavelength masks described in Section 4.4 before computing the CCF, removing the lowest-S/N pixels both globally and within local wavelength bins. Even after masking, however, the CCF retains velocity-dependent variance and covariance, especially near $v = 0\,\mathrm{km\,s^{-1}}$, because some low-S/N pixels associated with telluric absorption bands remain even after our double-masking procedure. We therefore adopt a Bayesian treatment that models the full one-dimensional CCF as the data vector. Building on the HRCCS retrieval framework that recasts the CCF as a likelihood (M. Brogi & M. R. Line 2019; N. P. Gibson et al. 2020), we extend it with molecule-specific kernels to capture the expected CCF morphology and an autoregressive AR(1) term to model interbin covariance directly in velocity space. We then use `MultiNest` to compute model evidences, and the resulting Bayes factors provide the basis for assessing molecular detections.

6. Bayesian Evidence Estimation of Atmospheric Signals

To determine when a species is detected, we apply Bayesian model comparison to the one-dimensional CCF, contrasting a null model with a signal model by incorporating the expected molecular signal from the planetary atmosphere, hereafter referred to as the "signal" model. Using `MultiNest`, we compute the evidences Z_{sig} and Z_{null}, where

$$Z_m = \int \mathcal{L}_m(\mathbf{y}|\theta_m)\,\pi_m(\theta_m)\,\mathrm{d}\theta_m, \tag{14}$$

with likelihood $\mathcal{L}_m$ for the CCF data $\boldsymbol{y}$ and prior π_m over parameters θ_m of model $m \in \{\mathrm{sig}, \mathrm{null}\}$. We compare the two

models via the Bayes factor B, calculated as

$$\log_{10} B = \log_{10} Z_{\rm sig} - \log_{10} Z_{\rm null}, \tag{15}$$

and we map $\log_{10} B$ to Jeffreys categories for qualitative statements.

6.1. Cross-correlation Function Data Vector and Noise Model

For each planet–molecule configuration, we start by generating $M = 100$ independent trials; in trial k we draw a new realization of the noise, process it through the simulation pipeline, and obtain a CCF array $\{y_i^{(k)}\}$ sampled at velocity bins $\{v_i\}$. This ensemble constitutes our Monte Carlo sample for that configuration. Each CCF spans $[-200,\ 200]\,\mathrm{km\,s^{-1}}$, sampled on $N = 401$ velocity bins, typically with a candidate peak near the expected total planetary velocity $v_{\rm tot}$ (Equation (4)) and, in some cases, a residual telluric feature near $0\,\mathrm{km\,s^{-1}}$. We then estimate the empirical dispersion across trials:

$$\sigma_i = \sqrt{\frac{1}{M-1}\sum_{k=1}^{M}\left(y_i^{(k)} - \bar{y}_i\right)^2}, \qquad \bar{y}_i = \frac{1}{M}\sum_{k=1}^{M} y_i^{(k)}, \tag{16}$$

where $y_i^{(k)}$ is the CCF value at velocity bin v_i in trial k. In practice, adjacent bins within a given CCF are correlated. The per-bin standard deviations σ_i, estimated across Monte Carlo realizations, quantify the empirical scatter at each velocity bin but do not encode the covariance between neighboring bins within a single CCF realization (Appendix B.1). Rather than estimating the full CCF covariance matrix $\boldsymbol{\Sigma}$ directly from the spectra (Appendix B.2), we approximate it by $\tilde{\boldsymbol{\Sigma}} = \boldsymbol{DRD}$, where $\boldsymbol{D} = \mathrm{diag}(\sigma_1, \ldots, \sigma_N)$ contains the per-velocity standard deviations and $\boldsymbol{R}$ is a stationary AR(1) correlation matrix with elements $R_{ij} = \hat{\rho}_{\rm w}^{|i-j|}$ (Appendix B.3). The lag-1 correlation coefficient $\hat{\rho}_{\rm w}$ is estimated from off-peak velocity regions only, excluding both the planetary signal and the telluric residual near zero velocity, then computed using a Yule–Walker estimator for a stationary AR(1) process and clipped to $|\hat{\rho}_{\rm w}| < 0.9$ (Appendix B.4).

To prevent local variance anomalies from disproportionately weighting the signal-bearing bins, we replace the empirical σ_i near $v_{\rm tot}$ and near $v = 0\,\mathrm{km\,s^{-1}}$ by a single robust scale $\tilde{\sigma}$, defined as the median of σ_i over off-peak velocities, while retaining the original σ_i elsewhere. The resulting standard-deviation array, together with $\hat{\rho}_{\rm w}$, is used in the AR(1) likelihood to account for correlated noise in velocity space.

6.2. Null and Signal Models

A straightforward approach would be to fit a Gaussian profile to the CCF maximum. However, such a fit would not address the telluric contamination discussed in Section 5. In addition, some of the species we study exhibit quasi-regular line spacings within a vibrational band, which generate secondary peaks in the CCF at characteristic lags; this is a generic consequence of structured-template autocorrelation in correlation analyses (e.g., for a signal processing example; A. Said et al. 2016). O_2 and CO_2 exhibit structured band patterns in the spectral regions considered here (J. T. Kiehl & T. Yamanouchi 1985; P. E. Martin & E. F. Barker 1932), which can produce side lobes in the CCF through template autocorrelation, as illustrated in Figure 5. By contrast, CH_4 and

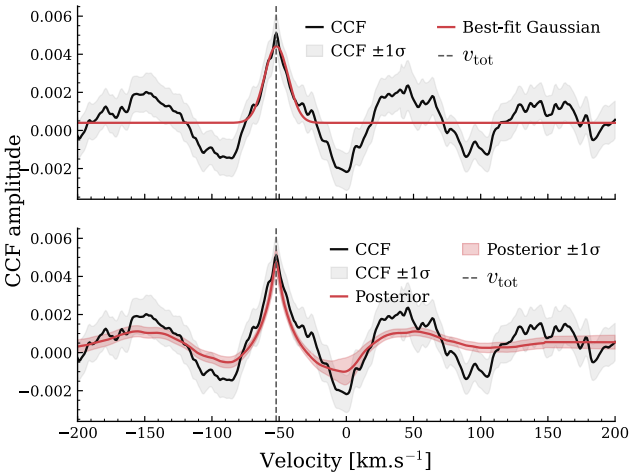


Figure 5. CCF for CO_2 on TRAPPIST-1 e corresponding to 40 stacked transits, fitted with two different models. Top: Gaussian + constant baseline fitted by bounded nonlinear least-squares (trust region reflective algorithm), minimizing the sum of squared residuals. It fails to capture the secondary lobes. Bottom: posterior predictive mean of the signal model, from our Bayesian framework. The molecule-specific kernel captures the full shape of the CCF, outperforming the simple Gaussian model.

H_2O possess dense and irregular spectra (e.g., R. J. Barber et al. 2006; J. Tennyson et al. 2013; S. N. Yurchenko & J. Tennyson 2014; S. N. Yurchenko et al. 2024), leading to a single dominant CCF maximum with no discernible secondary structure. A simple Gaussian fit, with its flat baseline, cannot capture the side lobes. The baseline then absorbs midscale features, biasing the recovered amplitude A toward lower values and reducing the inferred evidence. This behavior is illustrated in the top panel of Figure 5.

To address this, we introduce a molecule-specific model that more accurately represents the shape of the CCF. For the Bayesian comparison, both hypotheses (null and signal) share a quadratic baseline that captures the smooth, low-order curvature of the CCF across the $\pm 200\,\mathrm{km\,s^{-1}}$ range:

$$B(v) = y_0 + b(v - v_{\rm tot}) + c(v - v_{\rm tot})^2, \tag{17}$$

where y_0, b, and c are nuisance parameters and $v_{\rm tot}$ is the reference velocity defined in Equation (4).

Both models also include a zero-velocity nuisance component:

$$T(v) = A_{\rm tel} \exp\left(-\frac{v^2}{2\sigma_{\rm tel}^2}\right), \tag{18}$$

modeled as a Gaussian centered at zero velocity with free amplitude $A_{\rm tel}$ and width $\sigma_{\rm tel}$. This term captures localized CCF structure caused by noisy pixels in telluric absorption bands (Appendix A) and is treated as a nuisance component in both the signal and null hypotheses.

The null model is therefore

$$m_{\rm null}(v) = B(v) + T(v), \tag{19}$$

while the signal model adds a molecular kernel centered at the expected planetary velocity:

$$m_{\rm sig}(v) = B(v) + A\,K(v - v_{\rm tot}) + T(v), \tag{20}$$

where A is the signal amplitude. The kernel K depends on the molecule and is tabulated on the CCF velocity grid as a function of the lag $\Delta v = v - v_{\rm tot}$.

Operationally, the kernel is constructed as the autocorrelation of the molecular template $\mathcal{T}$:

$$K(\Delta v) \propto \int \mathcal{T}(u)\, \mathcal{T}(u + \Delta v)\, du. \tag{21}$$

K is evaluated on the same velocity grid as the CCF. In practice, the kernel is mean subtracted and normalized to unit ℓ_2 norm before fitting. Mean subtraction ensures that the kernel captures only structured features in the CCF and does not absorb any constant offset, which is modeled separately by the baseline. Unit ℓ_2 normalization fixes the overall scale of the kernel, so that the amplitude parameter A directly measures the strength of the molecular signal on a common scale across all species. Using this molecule-specific kernel instead of a simple Gaussian preserves the characteristic secondary lobes present in the CCFs of species with quasi-regular line spacings. The resulting improvement over a Gaussian model is illustrated in the bottom panel of Figure 5.

6.3. Priors

We choose weakly informative priors on the model parameters. In the implementation used for this work, the kernel centroid is fixed at the expected total planetary velocity $v_{\rm tot}$ (Equation (4)), and the kernel width is set by the template autocorrelation; we therefore do not fit additional centroid or stretch parameters.

1. *Amplitude.* From the Monte Carlo CCF ensemble we compute a per-velocity standard deviation σ_i (Section 6.1). We then define $\tilde{\sigma}$ as the median of σ_i over "off-peak" velocities, excluding both the planetary core and the telluric region (i.e., $|v - v_{\rm tot}| < 40\,{\rm km\,s^{-1}}$ and $|v| < 40\,{\rm km\,s^{-1}}$). For each molecule we introduce an amplitude scale

$$A_\sigma = f_{\rm mol}\, \tilde{\sigma}, \tag{22}$$

and adopt a half-normal prior

$$A \sim \mathrm{HalfNormal}(A_\sigma). \tag{23}$$

In this work we set $f_{\rm mol} = 7$ for all species.

2. *Baseline.* We place normal priors on the offset, slope, and curvature of the baseline:

$$\begin{aligned} y_0 &\sim \mathcal{N}(0,\, \tilde{\sigma}), \\ b &\sim \mathcal{N}\left(0,\, \frac{0.2A_\sigma}{\Delta v_{\rm span}}\right), \\ c &\sim \mathcal{N}\left(0,\, \frac{0.1A_\sigma}{\Delta v_{\rm span}^2}\right), \end{aligned} \tag{24}$$

where $\Delta v_{\rm span}$ denotes the full velocity span of the CCF.

3. *Telluric component.* The telluric amplitude $A_{\rm tel}$ is assigned a zero-mean normal prior:

$$A_{\rm tel} \sim \mathcal{N}(0,\, \tilde{\sigma}), \tag{25}$$

while the width is given a log-uniform prior:

$$\sigma_{\rm tel} \sim \mathcal{LU}(5,\, 80). \tag{26}$$

6.4. Likelihood and Nested Sampling

All priors are built via inverse cumulative distribution function transforms from unit-hypercube draws $u \sim \mathcal{U}(0, 1)$ in `MultiNest` and numerically clipped to $[10^{-9},\ 1 - 10^{-9}]$ to avoid infinities. Transforms are implemented with `SciPy` (P. Virtanen et al. 2020). For a parameter θ we do the following.

(i) Normal prior. For $\theta \sim \mathcal{N}(\mu, \sigma^2)$

$$\theta = \mu + \sigma\sqrt{2}\ \mathrm{erf}^{-1}(2u - 1), \tag{27}$$

where erf^{-1} is the inverse error function.

(ii) Half-normal prior. For a nonnegative parameter with scale σ:

$$\theta = \sigma\sqrt{2}\ \mathrm{erf}^{-1}(u), \qquad \theta \geqslant 0. \tag{28}$$

(iii) Log-uniform prior. For bounds $[x_{\rm min}, x_{\rm max}]$:

$$\theta = x_{\rm min}\left(\frac{x_{\rm max}}{x_{\rm min}}\right)^u. \tag{29}$$

These mappings ensure that `MultiNest` samples the intended prior measures directly from u while maintaining numerical stability in the likelihood evaluation.

The likelihood is derived from the multivariate normal distribution:

$$\begin{aligned} \ln \mathcal{L}(\boldsymbol{y}|\boldsymbol{\theta}) = -\frac{1}{2}[&\ln(\det(\boldsymbol{\Sigma})) \\ &+ (\boldsymbol{y} - \boldsymbol{m}(\boldsymbol{\theta}))^\top \boldsymbol{\Sigma}^{-1} (\boldsymbol{y} - \boldsymbol{m}(\boldsymbol{\theta})) \\ &+ N \ln(2\pi)], \end{aligned} \tag{30}$$

where $\boldsymbol{y} = (y_1,\ldots,y_N)^\top$ is the observed CCF sampled on the velocity grid $\{v_i\}_{i=1}^N$, $\boldsymbol{m}(\boldsymbol{\theta})$ is the model prediction evaluated on the same grid, N is the number of velocity bins, $\boldsymbol{\Sigma}$ is the $N \times N$ covariance matrix of the residual vector, and $\det(\boldsymbol{\Sigma})$ is the determinant of $\boldsymbol{\Sigma}$.

Under the AR(1) approximation (Section 6.1 and Appendix B.3) and using the clipped Yule–Walker estimator $\hat{\rho}_{\rm w}$ derived in Appendix B.4, the likelihood admits the closed-form expression

$$\begin{aligned} \ln \mathcal{L}(\boldsymbol{y}|\boldsymbol{\theta},\, \hat{\rho}_{\rm w}) = &-\sum_{i=1}^{N} \ln \sigma_i - \frac{N-1}{2} \ln\left(1 - \hat{\rho}_{\rm w}^2\right) \\ &- \frac{1}{2}\left[z_1^2 + \frac{1}{1 - \hat{\rho}_{\rm w}^2} \sum_{i=2}^{N} (z_i - \hat{\rho}_{\rm w} z_{i-1})^2 \right] \\ &- \frac{N}{2} \ln(2\pi), \end{aligned} \tag{31}$$

where $z_i = [y_i - m_i(\boldsymbol{\theta})]/\sigma_i$ denotes the standardized residual at velocity bin v_i. It renders the likelihood computationally tractable within nested sampling while retaining the dominant velocity-bin correlation structure of the CCF. A full description and justification of the correlation model and estimator is provided in Appendix B.

We fit the null and atmospheric-signal models with `MultiNest` via `PyMultiNest` (J. Buchner 2016), obtaining posterior samples and the log evidence $\ln Z$ for each model, and we compute the Bayes factor defined in Equation (15).

As a basic calibration test of the Bayesian framework, we also applied the same analysis to null templates containing no injected planetary signal. In these cases, the model comparison consistently favored the null hypothesis, with Bayes factors indicating no spurious preference for the signal model. This provides an initial validation that the framework is not predisposed to favor the signal model in the absence of injected signal.

7. Application of the Detection Framework

We apply our analysis pipeline[14] to the 18 planets retained after the visibility and radius cuts described in Section 2. For each planet, we evaluate the detectability of H_2O, CH_4, CO_2, and O_2, using six cumulative transit counts corresponding to 3, 10, 25, 50, 75, and 100 transits, adopting 100 transits as a practical upper limit.

For each planet–molecule pair and each transit count, we generate $M \geqslant 100$ independent CCF realizations. We compute the Bayes factor for each one and use the median $\log_{10} B$ over these M draws as the representative detection strength. The Monte Carlo stability of this median is assessed using the stopping criterion described in Appendix C. We then estimate the minimum number of transits required to reach "decisive" evidence (Jeffreys scale; $\log_{10} B \geqslant 2.0$), by linearly interpolating the median Bayes factors obtained across the transit-count grid.

All planets that yield decisive evidence for at least one gas in fewer than 100 transits are listed in Figure 6. This criterion reduces the sample from 18 to eight planets. Figure 6 compiles these estimates and provides the most planning-relevant result: a concise view of the transit requirement for each gas and retained target. As a rough measure of observing cost, we also report in each cell the corresponding idealized number of 7 hr observing nights. This quantity is computed as

$$N_{\rm nights} = \frac{2 N_{\rm transits} T_{14}}{7\ {\rm hr}}, \tag{32}$$

where T_{14} is the transit duration and the factor of 2 corresponds to the simulated observing sequence spanning one T_{14} in transit plus an equal out-of-transit baseline. The resulting $N_{\rm nights}$ values are rounded up to the nearest integer. They should be interpreted as idealized observing-night equivalents, not as real scheduling estimates, since they do not include, e.g., weather losses and seasonal constraints. We discuss their implications in Section 8.1.

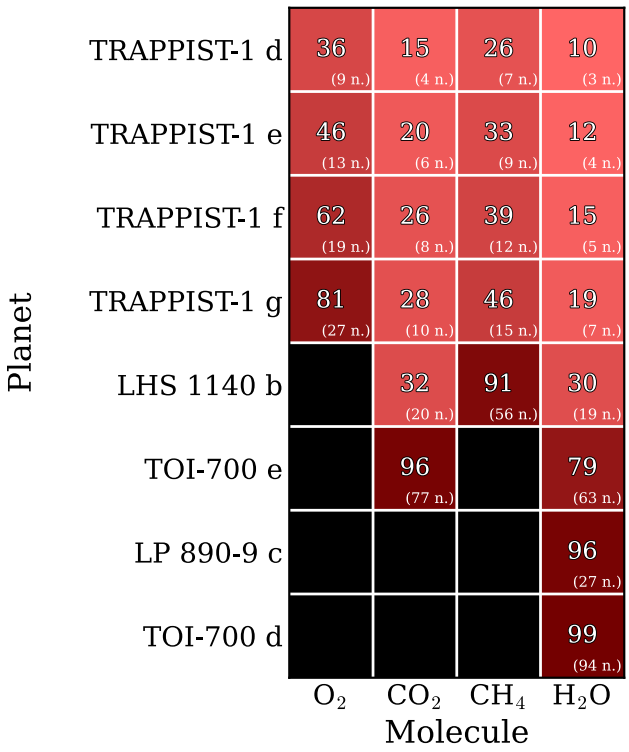


Figure 6. Estimated minimum number of transits required for decisive evidence ($\log_{10} B \geqslant 2.0$) of each gas with ANDES within our framework. Planets are ordered from top to bottom by (i) number of detectable molecules, and (ii) smaller total required transits (sum over detected molecules). Empty cells indicate that a decisive detection cannot be achieved in 100 transits under the assumptions adopted here. The number in parentheses gives the approximate equivalent observing time in 7 hr nights, rounded up to the nearest integer, and represents idealized time only; it does not include weather or seasonal constraints.

8. Results and Discussion

8.1. Main Detectability Results

From the initial pool of 70 targets in our sample, we exclude 29 nontransiting ones, 11 that are rejected by our screening proxy based on the adopted 20° altitude criterion, and 12 on the basis of planetary radius. Among the remaining 18 planets, eight meet the Jeffreys decisive detection threshold for at least one molecule within 100 transits. These final detectability estimates are summarized in Figure 6, which provides the main synthesis of our results. Within the assumptions adopted here, H_2O emerges as the most accessible species, meeting the detectability criterion for all eight planets in fewer than 100 transits. CO_2 is detectable for six planets and CH_4 is detectable for five, while O_2, detectable for four targets, proves the most challenging.

The TRAPPIST-1 system yields particularly favorable results, with all four molecules detectable on each of the four planets considered. Among them, TRAPPIST-1 d emerges as the most promising target overall in our ranking, requiring the fewest transits for every molecule and reaching full detectability within 36 transits. Three molecules are also detectable on LHS 1140 b within the 100-transit limit, although the required transit counts remain operationally difficult.

First, the planet-to-planet differences in detectability are predominantly explained by variations in scale height. The amplitude of individual planetary lines varies approximately with the atmospheric scale height, as $\Delta D \propto H R_{\rm p}/R_\star^2$, where $H = kT/(\mu g)$ increases with temperature and decreases with gravity and mean molecular weight (S. Seager & D. D. Sasselov 2000). This explains why planets with higher temperature and lower gravity, such as TRAPPIST-1 d, yield stronger features than cooler, higher-gravity planets like TRAPPIST-1 e.

[14] The framework developed in this work, `ANDES-Forecast`, is publicly available at https://github.com/EvannKurzawa/ANDES-Forecast.

Second, the contrast between the molecular detectability patterns in, e.g., the TRAPPIST-1 and LHS 1140 systems is instead primarily driven by the spectral energy distributions of their host stars. CO_2 absorption is probed mainly near 1.6 μm, whereas CH_4 and H_2O draw much of their information from red optical and NIR bands. Cooler stars like TRAPPIST-1 emit a larger fraction of their energy in the red optical and NIR than earlier M dwarfs such as LHS 1140, leading to a higher photon budget in the relevant CH_4 and H_2O bands. Synthetic atmosphere models confirm that late M dwarfs concentrate a larger share of their flux at longer wavelengths, with flux escaping primarily through the *J* and *H* bands in that order of decreasing strength (F. Allard & P. H. Hauschildt 1995). As a result, CH_4 and H_2O are easier to detect in TRAPPIST-1 than in the earlier-type system LHS 1140, even though CO_2 detectability remains comparable across both.

Finally, although TOI-700 d, TOI-700 e, and LP 890-9 c (also known as SPECULOOS-2 c) reach a decisive detection within the 100-transit limit adopted here, the required number of transits remains large enough to make such observations operationally impractical.

8.2. Comparison with Previous Studies

Establishing direct comparisons with previous studies is challenging. While a limited number of works have explored the potential of the ELT (or other extremely large telescopes) for characterizing the atmospheres of potentially habitable rocky planets around M dwarfs (e.g., F. Wunderlich et al. 2020; M. H. Currie et al. 2023), these typically consider hypothetical planets at distances that differ from those of our sample (often 5–15 pc). Most of these studies targeted individual absorption bands, and none specifically investigated the performance of ANDES. Our comparisons should therefore be interpreted as approximate contextual checks rather than as strict one-to-one validations.

For comparison purposes only, we provide in Appendix D a band-limited version of our analysis for TRAPPIST-1 e, together with the corresponding transit requirements for selected molecular bands. This appendix uses the heuristic threshold $\log_{10} B = 5.43$ solely to facilitate comparison with studies reporting 5σ estimates; these values are not used for the main target rankings or for the transit requirements shown in Figure 6.

F. Wunderlich et al. (2020) explored a range of atmospheric scenarios for TRAPPIST-1 e and f, including CO_2-rich cases, and estimated the number of transits required for a 5σ detection in several individual spectral bands. For the O_2 band at 1.24–1.30 μm, they reported that up to 910 transits could be required. Applying our band-limited mode to TRAPPIST-1 e over the same O_2 band (Appendix D; Table D1), we do not reach the heuristic "5σ" threshold within 300 transits. This remains qualitatively consistent with the conclusion that O_2 is extremely challenging to detect in transmission, although the numerical values cannot be compared directly because of differences in atmospheric assumptions, noise treatment, and detection metrics. F. Wunderlich et al. (2020) also reported 26 transits for CH_4 in the 2.12–2.50 μm band; however, this wavelength interval lies outside the range retained in our ETC-based simulations.

Later, M. H. Currie et al. (2023) simulated transmission spectroscopy of an Earth-like planet transiting an M dwarf, with an orbital configuration analogous to TRAPPIST-1 e. They reported that the ELT could detect CO_2 at 1.56 μm in 34 transits, CH_4 at 1.6 μm in 33 transits, O_2 at 1.27 μm in 200 transits, and H_2O at 0.9 μm in >300 transits (all at a 5σ significance level). Using our band-limited mode applied to TRAPPIST-1 e up to 300 transits, we find that CO_2 at 1.56–1.62 μm reaches our heuristic "5σ" threshold after 151 transits, while CH_4 at 1.62–1.70 μm, O_2 at 1.24–1.30 μm, and H_2O at 0.90–0.98 μm do not reach this threshold within 300 transits. Overall, the comparison remains qualitatively consistent in identifying CO_2 as one of the most accessible of these band-limited cases and H_2O as very challenging in the 0.9 μm band, but our transit requirements are generally less favorable.

The numerical discrepancies with previous estimates likely arise in part because our simulations adopt the most recent ANDES ETC outputs, which reflect an updated instrumental design with lower throughput, and therefore lower S/N, in some wavelength regions. We propagate this updated S/N scale into the simulated spectra by locally rescaling the dense v.3.2 wavelength structure to the v.5.2 normalization and interpolating the result onto a constant-*R* grid. This treatment of the ETC outputs differs from both the simpler feature-based S/N estimates of F. Wunderlich et al. (2020) and the SPECTR-based simulated observations of M. H. Currie et al. (2023), who use a separate implementation of the ELT–instrument noise budget.

E. Palle et al. (2025) presented an ANDES forward-modeling estimate for TRAPPIST-1 d and reported that a wet N_2-dominated atmosphere containing 400 ppm CO_2 could be recovered at $>12\sigma$ in five transits under photon-limited assumptions. This result is broadly consistent with the idea that molecular absorption features in TRAPPIST-1 d could be accessible to ANDES under optimistic assumptions. A direct numerical comparison, however, is difficult. The E. Palle et al. (2025) calculation uses a multispecies atmospheric template and a peak-based cross-correlation significance, whereas our analysis treats each absorber separately and uses Bayesian model comparison with a correlated-noise CCF likelihood. In our framework, H_2O and CO_2 reach decisive evidence for TRAPPIST-1 d within 15 transits, while CH_4 requires 26 transits. The difference likely reflects several conservative aspects of our setup: the use of the updated ETC v.5.2 normalization, the absence of seeing-limited *K*-band information, and the use of a Bayesian evidence metric with correlated CCF noise.

Finally, comparison with previous target-prioritization studies reveals strong convergence on the most amenable targets for atmospheric characterization. Both M. L. Hill et al. (2023) and A. Bohl et al. (2026) identify TRAPPIST-1 d as one of the most favorable habitable-zone planets, consistent with our findings, where TRAPPIST-1 d also ranks highest (see Figure 6). In our framework, the remaining potentially habitable TRAPPIST-1 planets (e, f, and g) follow closely, similar to the sequence reported by A. Bohl et al. (2026). Other planets that appear prominently in at least one of these works, as well as in ours, include LHS 1140 b, TOI-700 d, and LP 890-9 c, reinforcing their status as strong secondary candidates. However, the low density of LHS 1140 b may indicate a water world composition instead of a purely rocky one (C. Cadieux et al. 2024a; M. Damiano et al. 2024), although the planet might still retain habitable conditions on its surface.

8.3. Preliminary JWST Results for These Targets

Nearly all of the planets identified in our final sample have been or will be observed by the JWST, and these early results provide valuable context to test the assumptions of our atmospheric modeling. Initial JWST observations appear inconsistent with significant atmospheres on most warm to hot rocky exoplanets around M dwarfs (e.g., N. H. Allen et al. 2025; M. Fortune et al. 2025; M. Gillon et al. 2025; R. Luque et al. 2025; E. A. Meier Valdés et al. 2025; but see also A. Gressier et al. 2024; P. C. August et al. 2025; A. Bello-Arufe et al. 2025), but it is still unclear whether this trend extends to the temperate population (C. Cadieux et al. 2024b; M. Damiano et al. 2024; N. Espinoza et al. 2025; A. Glidden et al. 2025; C. Piaulet-Ghorayeb et al. 2025).

For TRAPPIST-1 d, our top-ranked target, JWST/NIRSpec transmission spectra disfavor a modern Earth-like, cloud-free atmosphere like the one we model in this work (C. Piaulet-Ghorayeb et al. 2025). Instead, the data are consistent with either a tenuous Mars-like atmosphere, a high-altitude Venus-like cloud deck, or no atmosphere at all. In contrast, existing JWST observations of TRAPPIST-1 e rule out H_2-dominated atmospheres but remain consistent with high-mean-molecular-weight atmospheres, including N_2-dominated compositions with trace CO_2 or CH_4 (N. Espinoza et al. 2025; A. Glidden et al. 2025). Meanwhile, LHS 1140 b has a featureless or weakly sloped transmission spectrum that disfavors a clear H_2–He-dominated envelope and is consistent with a high-mean-molecular-weight atmosphere or water-rich scenario (C. Cadieux et al. 2024b; M. Damiano et al. 2024).

Taken together, early JWST results suggest that modern, cloud-free, Earth-like atmospheres remain plausible for nearly all targets in our sample, including LHS 1140 b and TRAPPIST-1 e. While our simulations present lower limits on the number of transits required for atmospheric detection with ANDES, the ongoing synergy between JWST and the ELT will be crucial in refining our understanding of atmospheric diversity and biosignature detectability on rocky exoplanets.

8.4. Important Caveats

Below, we summarize the most relevant caveats.

1. *Telluric correction.* We assume that telluric absorption lines can be removed down to the photon-noise level. This remains a significant challenge, particularly in the NIR where telluric contamination is most severe and time variable. Current methods such as `molecfit` (W. Kausch et al. 2015; A. Smette et al. 2015) and data-driven principal component analysis (PCA; e.g., A. Meech et al. 2022) can achieve excellent results under favorable conditions, but full correction at the noise limit is rarely attained. The achievable precision depends on the instrument stability, the accuracy of the telluric models, and the temporal variability of the atmosphere during the observing sequence. Residual telluric structures may therefore introduce additional systematic noise that increases the effective number of required transits.
2. *Planet–star spectral separation.* We assume that the planetary spectrum can be isolated from the stellar and telluric signals without degrading the exoplanetary features. This is a strong assumption, especially for the terrestrial planets considered here, whose radial-velocity drift during transit is typically only a few tenths to a few kilometers per second. Traditional detrending techniques, including SYSREM (O. Tamuz et al. 2005; T. Mazeh et al. 2007) or PCA-based filtering, rely on the assumption that the planetary lines shift sufficiently in velocity space to avoid being removed together with the quasi-stationary stellar and telluric lines. In practice, this assumption can fail for terrestrial systems, causing significant attenuation of the planetary signal. To address this limitation, N. Piskunov et al. (2025) recently introduced Transmission Spectroscopy Decomposition, an inverse-problem framework that simultaneously solves for the stellar, telluric, and planetary spectra directly from the time series, thereby avoiding template cross correlation and minimizing signal loss. Although promising, the method requires resolving the planet's velocity change during transit and may therefore remain challenging for slowly orbiting rocky planets. Complementary approaches based on machine learning are also emerging; for instance, R. D. Kjærsgaard et al. (2023) proposed Telluric AUtoencoder, a neural-network-based telluric and stellar correction framework that can disentangle overlapping spectral components without relying on linear decomposition. These techniques represent an important step beyond classical detrending but have yet to be extensively validated in the low-velocity, low-S/N regime relevant to temperate terrestrial planets.
3. *Clouds and hazes.* We assume cloud-free atmospheres, although clouds and hazes may be present on these planets (e.g., J. Yang et al. 2013), potentially muting spectral features and complicating atmospheric characterization (J. Lustig-Yaeger et al. 2019). High-resolution transmission spectroscopy, however, probes the cores of individual lines, which form at low pressures, and is therefore less sensitive to clouds and hazes than its low-resolution counterpart (e.g., JWST; S. Gandhi et al. 2020).
4. *Stacking and noise scaling.* We assume that stacking multiple transits improves the S/N as $\sqrt{N_{\rm transits}}$, but it is unclear whether this will be true for ELT/ANDES. The effective scaling will need to be established empirically during commissioning and early surveys; until then, our estimates should be considered optimistic lower limits.
5. *Stellar contamination.* We do not explicitly account for stellar variability, active regions, or flares, which are common among M dwarfs. Such activity can alter the effective photospheric spectrum during transit and bias molecular detections (the so-called transit light source effect; B. V. Rackham et al. 2018; A. D. Rathcke et al. 2025). While high-resolution spectroscopy provides some mitigation by leveraging the planet's orbital motion to disentangle the planetary and stellar components (P. W. Cauley et al. 2018), the impact of stellar contamination on high-resolution transmission spectroscopy of M dwarf systems remains poorly constrained.
6. *Single-species treatment.* We compute transmission spectra for one target absorber at a time rather than performing full multispecies radiative transfer. Molecular overlap and masking are therefore neglected, so the

reported transit requirements should be interpreted as optimistic estimates for isolated species.

7. *Screening proxy versus true observability.* Our target selection and estimated transit counts are based on a simplified altitude-based visibility proxy rather than a full transit-by-transit observability analysis. The sampled epochs used to evaluate the altitude criterion and barycentric correction are not tied to actual transit times.
8. *Additional simplifying assumptions.* These include circular orbits, Earth-like atmospheric composition and surface pressure, and a negligible readout overhead compared to the 10 minute integration time. We also neglect potential instrument systematics. In addition, because we apply the optimal barycentric correction to maximize Doppler separation between exoplanetary and telluric spectral lines, our results represent an optimistic scenario. In practice, observers are encouraged to schedule observations such that the exoplanet spectral lines are Doppler shifted away from the noisy telluric lines in order to increase the S/N of molecular features.

Overall, these assumptions imply that our results likely underestimate the true number of transits required for detection. The goal of this work is to provide optimistic estimates of molecular detectability with ELT/ANDES under idealized observing conditions, and to estimate the minimum transit counts required for the most favorable transiting targets. Future efforts could aim to relax these assumptions and refine the physical modeling and pipeline implementation, and we encourage the community to focus on these challenges before ANDES starts operations, to maximize scientific return.

9. Summary and Conclusions

We developed a framework to estimate ELT/ANDES transit requirements for detecting four key atmospheric molecules, including two biosignature gases, on potentially habitable exoplanets. For each planet, we modeled a cloud-free, Earth-like, two-layer atmosphere and simulated the transmission spectra with `petitRADTRANS`, adding realistic noise with the ANDES ETC. We cross correlated the resulting spectra with model templates, and we quantified the detection significance using a Bayesian framework featuring a custom kernel scheme to emulate the CCFs and an autoregressive AR(1) model to mitigate correlation across velocity bins. We then applied the full pipeline to the most favorable planets in our sample, which yielded evidence scores and the required transit numbers to reach detectability.

Our simulations indicate that water vapor and carbon dioxide are the most accessible species for ground-based detection with ANDES, requiring fewer than $\sim$20 transits for the most favorable targets (e.g., TRAPPIST-1 d and e). Methane is moderately accessible, while oxygen remains the most challenging species to detect. Eight planets show at least one molecule detectable within $\lesssim$100 transits: TRAPPIST-1 d, e, f, and g; LHS 1140 b; LP 890-9 c; and TOI-700 d and e. TRAPPIST-1 d emerges as the most favorable target overall, with all four gases detectable in fewer than 36 transits. These results should be regarded as optimistic lower limits, contingent on photon-noise performance, perfect telluric and stellar removal, and cloud-free atmospheres.

In summary, this study highlights the potential of ELT/ANDES for atmospheric characterization of nearby transiting terrestrial exoplanets in the photon-limited regime. Under these assumptions, the detection of key molecules central to the search for life, such as CO_2, CH_4, and H_2O on the TRAPPIST-1 planets may be feasible within campaigns of $\lesssim$30 transits. Achieving this performance will require substantial progress in telluric and stellar contamination removal, which remain the dominant barriers to reaching the photon-limited regime, particularly for slowly moving planets, where spectral disentanglement is most challenging.

Finally, although this work focuses on transiting planets, our results also highlight the importance of complementary searches around nearby nontransiting systems. Transmission spectroscopy benefits from a well-defined observing geometry, but it is restricted to the small subset of habitable-zone planets that transit and, as shown here, may require large observing campaigns even under optimistic assumptions. Reflected-light observations combining high-contrast imaging and high-resolution spectroscopy offer an alternative route for ANDES, because they can target the nearest habitable-zone planets regardless of whether they transit (I. Snellen et al. 2015; D. Mawet et al. 2017; J. Wang et al. 2017; S. R. Vaughan et al. 2024; E. Palle et al. 2025). Such systems may therefore be at least as important as transiting planets for future ELT biosignature searches, and deserve a dedicated analysis beyond the transmission-spectroscopy study presented here.

Acknowledgments

E.K.F. gratefully acknowledges the Région Auvergne-Rhône-Alpes and the Fondation Ailes de France for their financial support. This research was carried out at the Jet Propulsion Laboratory, California Institute of Technology, under a contract with the National Aeronautics and Space Administration (80NM0018D0004). Part of the High Performance Computing resources used in this investigation were provided by funding from the JPL Information and Technology Solutions Directorate. We also thank the ANDES ETC team, and in particular Nicoletta Sanna and Alessandro Marconi, for their helpful clarifications regarding the ETC outputs and the evolving ANDES instrumental assumptions.

This research has made use of the NASA Exoplanet Archive, which is operated by the California Institute of Technology, under contract with the National Aeronautics and Space Administration under the Exoplanet Exploration Program. It has also made use of the SIMBAD database, operated at CDS, Strasbourg Astronomical Observatory, France; the Habitable Worlds Catalog (HWC; PHL @ UPR Arecibo 2026); the DACE platform (Data & Analysis Center for Exoplanets) operated at the University of Geneva within the Swiss National Centre of Competence in Research (NCCR); the Keeper knowledge base of the Max Planck Digital Library; the TESS Input Catalog; the USNO-B Catalog; data products from the Two Micron All Sky Survey (2MASS); and public resources provided by the European Southern Observatory (ESO), including the ELT construction proposal, the ANDES documentation, and the ANDES Exposure Time Calculator.

Software: `Astropy` (Astropy Collaboration 2022), `SciPy` (P. Virtanen et al. 2020), `PyAstronomy` (S. Czesla et al. 2019), `barycorrpy` (S. Kanodia & J. Wright 2018), `petitRADTRANS` (P. Mollière et al. 2019), `SPRIGHT` (H. Parviainen et al. 2024), `PyMultiNest` (J. Buchner 2016), ANDES Exposure Time Calculator (N. Sanna et al. 2024), `ANDES-Forecast` (https://github.com/EvannKurzawa/ANDES-Forecast).

Appendix A
Zero-velocity Artifact

We employ a one-dimensional CCF analysis, which in several cases reveals a narrow peak at $v \approx 0\,\mathrm{km\,s^{-1}}$ in the observer frame. This manifests as either a positive or negative peak, as shown in Figure A1, and accounts for most of the variance near zero lag. Consequently, "far-from-signal" standard-deviation estimates cease to be representative of the baseline, and classical S/N metrics become unreliable.

This zero-velocity behavior is a consequence of how telluric absorption enters our simulations. We assume ideal telluric correction at the spectral level and do not inject a deterministic residual telluric spectrum; however, the ANDES ETC assigns lower S/N to wavelengths affected by telluric absorption. The effect can be understood as follows.

1. *Stationarity in the observer frame.* Wavelengths affected by telluric absorption are fixed in the observer's rest frame. Even after ideal telluric correction, these wavelengths retain larger uncertainties in the ETC noise model. Their noise contribution can therefore produce enhanced CCF variance near $v \approx 0\,\mathrm{km\,s^{-1}}$, including localized positive or negative peaks in individual realizations.
2. *Molecular overlap with the target gases.* The dense line lists of O_2, H_2O, CO_2, and CH_4 overlap strongly with Earth's atmosphere, so even small residual mismatches can mimic the spectral patterns used to search for exoplanet signals.

We perform the following diagnostics, which directly link the zero-velocity feature to telluric-noise effects.

1. *Velocity shift experiment.* The observed spectrum can be decomposed into contributions from the star, the planet, and Earth's atmosphere. To test their individual contributions, we artificially shift each component by arbitrary velocities: $53\,\mathrm{km\,s^{-1}}$ for the telluric spectrum, $29\,\mathrm{km\,s^{-1}}$ for the stellar spectrum, and $97\,\mathrm{km\,s^{-1}}$ for the planetary spectrum. In the resulting CCFs, the spurious feature shifted exactly with the telluric component ($53\,\mathrm{km\,s^{-1}}$), whereas structures associated with the stellar and planetary spectra did not follow. This isolates the terrestrial component as the origin of the artifact.
2. *Monte Carlo uncertainty analysis.* We construct the CCF standard-deviation array by repeating the calculation hundreds of times with Monte Carlo sampling. This reveals a localized peak in uncertainty centered at $0\,\mathrm{km\,s^{-1}}$, consistent with excess variance introduced by telluric features, supporting the interpretation of a telluric origin.

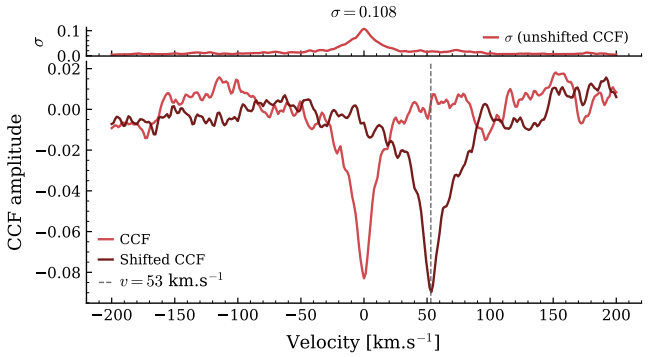


Figure A1. CCFs for Kepler-1649 c with low-S/N pixel masking. Two CCFs are shown: the standard one, and one where the stellar, planetary, and telluric contributions are shifted independently. In the shifted case, the feature follows the telluric-noise contribution at $53\,\mathrm{km\,s^{-1}}$, as discussed in Appendix A. For illustration, we display the standard-deviation curve from the unshifted case, which shows a pronounced uncertainty peak at $0\,\mathrm{km\,s^{-1}}$. This supports the interpretation that the feature is caused by noisy pixels associated with telluric absorption bands.

A representative example of these two diagnostics is shown in Figure A1.

In the Bayesian analysis, this zero-velocity CCF structure is marginalized over by including a Gaussian nuisance component centered at zero velocity in both the signal and null models.

Appendix B
Correlation between Cross-correlation Function Velocity Bins: Origin, Ideal Treatment, and Our Practical Approach

Here we derive the CCF correlation structure, using classical time-series results on AR(1) processes (e.g., J. D. Hamilton 1994; D. S. Wilks 2011).

B.1. Correlation Origin and Behavior with Δv

Let the continuum-normalized spectrum at pixel index p be

$$d_p = s_p + n_p, \tag{B1}$$

with signal s_p and noise n_p (zero mean). For a velocity v, we correlate the data with a Doppler-shifted template $t_p(v)$, applying inverse-variance weights w_p to each pixel:

$$y(v) = \sum_{p=1}^{P} \underbrace{[w_p\, t_p(v)]}_{\phi_p(v)} d_p = \boldsymbol{\phi}(v)^{\top}\boldsymbol{d}. \tag{B2}$$

Here, $\boldsymbol{\phi}(v) \in \mathbb{R}^P$ is the velocity-dependent weight vector, $y(v)$ is the CCF between the data and the template, and $\boldsymbol{d}$ is the data vector. Sampling $y(v)$ on a velocity grid $\{v_i\}_{i=1}^{N}$ yields the CCF vector $\boldsymbol{y} \in \mathbb{R}^N$ with components $y_i = y(v_i)$. Because nearby weight vectors $\boldsymbol{\phi}(v_i)$ and $\boldsymbol{\phi}(v_j)$ are shifted versions of the same template, they overlap strongly. Using the covariance of linear combinations of a random vector, this overlap couples y_i and y_j:

$$\mathrm{Cov}(y_i, y_j) = \mathrm{Cov}\left(\boldsymbol{\phi}_i^{\top}\boldsymbol{d},\, \boldsymbol{\phi}_j^{\top}\boldsymbol{d}\right) = \boldsymbol{\phi}_i^{\top}\boldsymbol{C}_d\,\boldsymbol{\phi}_j, \tag{B3}$$

where $\boldsymbol{C}_d = \mathrm{Cov}(\boldsymbol{d})$ is the data covariance matrix, and $\boldsymbol{\phi}_i = \boldsymbol{\phi}(v_i)$.

If we consider white noise (same variance σ^2 for each pixel, no correlations) for the data, then the data covariance matrix is diagonal: $\boldsymbol{C}_d = \sigma^2\mathbf{I}$, and hence

$$\mathrm{Cov}(y_i, y_j) = \sigma^2\,\boldsymbol{\phi}_i^{\top}\boldsymbol{\phi}_j, \quad \mathrm{Var}(y_i) = \sigma^2\|\boldsymbol{\phi}_i\|^2. \tag{B4}$$

Using the Pearson correlation coefficient, the correlation between CCF bins is

$$\rho_{ij} = \frac{\mathrm{Cov}(y_i, y_j)}{\sqrt{\mathrm{Var}(y_i)\,\mathrm{Var}(y_j)}} = \frac{\boldsymbol{\phi}_i^{\top}\boldsymbol{\phi}_j}{\|\boldsymbol{\phi}_i\|\,\|\boldsymbol{\phi}_j\|}. \tag{B5}$$

Thus, ρ_{ij} is the normalized dot product between two weight vectors, such that $\rho_{ii} = 1$. If $\boldsymbol{\phi}_j$ is a velocity-shifted version of

ϕ_i, the correlation is the normalized overlap of the template with itself at that shift. Writing a continuous weight function $\phi(x)$ and a velocity lag $\Delta v = v_j - v_i$, the continuum analog of Equation (B5) is the normalized inner product:

$$\rho(\Delta v) = \frac{\int \phi(x)\phi(x - \Delta v)dx}{\int \phi(x)^2 dx}. \tag{B6}$$

For a Gaussian-shaped weight, let $\phi(x) = \exp[-x^2/(2\sigma^2)]$. Then

$$\int \phi(x)\phi(x - \Delta v)\, dx = \int \exp\left[-\frac{x^2 + (x - \Delta v)^2}{2\sigma^2}\right] dx, \tag{B7}$$

$$= \exp\left[-\frac{(\Delta v)^2}{4\sigma^2}\right] \int \exp\left[-\frac{(x - \Delta v/2)^2}{\sigma^2}\right] dx, \tag{B8}$$

and since shifting the center of a Gaussian does not change its total area, the integral is independent of Δv. Therefore

$$\boxed{\rho(\Delta v) \propto \exp\left[-\frac{(\Delta v)^2}{4\sigma^2}\right].} \tag{B9}$$

In practice, our kernel is the autocorrelation of the molecular template, not an ideal Gaussian. For CH_4 and H_2O, the shape is close to Gaussian, while for CO_2 and O_2 it resembles a Gaussian with secondary lobes (see Section 6.2). Nevertheless, $\rho(\Delta v)$ still decays with increasing Δv, as expected from the diminishing overlap between shifted kernels, with the Gaussian case of Equation (B9) providing a useful approximation to the general behavior.

B.2. Ideal Treatment: Full Covariance across Velocity Bins

For a given realization, let $\boldsymbol{y} \in \mathbb{R}^N$ denote the CCF vector sampled on the N-point velocity grid, and let $\boldsymbol{m}(\boldsymbol{\theta})$ be the corresponding model prediction, with ith component $m_i(\boldsymbol{\theta})$. Since the CCF bins are linear combinations of Gaussian noise contributions at the pixel level, they are themselves Gaussian. The correct distribution for a vector of correlated Gaussian variables is the multivariate normal distribution, with covariance matrix $\boldsymbol{\Sigma}$. The likelihood is then the standard multivariate normal form (e.g., C. M. Bishop 2006):

$$\ln \mathcal{L}(\boldsymbol{y}|\boldsymbol{\theta}) = -\frac{1}{2}[\ln(\det(\boldsymbol{\Sigma})) + (\boldsymbol{y} - \boldsymbol{m}(\boldsymbol{\theta}))^\top \boldsymbol{\Sigma}^{-1} \times (\boldsymbol{y} - \boldsymbol{m}(\boldsymbol{\theta})) + N \ln(2\pi)], \tag{B10}$$

where $\det(\boldsymbol{\Sigma})$ corresponds to the determinant of $\boldsymbol{\Sigma}$. From Equation (B3), let us consider multiple exposures indexed by e. Each exposure has a matrix $\boldsymbol{F}^{(e)}$, whose ith row is $\boldsymbol{\phi}^{(e)}(v_i)^\top$, and a noise covariance matrix $\boldsymbol{C}^{(e)}$ for its spectrum. The combined CCF covariance is then

$$\boldsymbol{\Sigma} = \sum_e \boldsymbol{F}^{(e)} \boldsymbol{C}^{(e)} \boldsymbol{F}^{(e)\top}. \tag{B11}$$

This expression follows directly from the linearity of the CCF, and therefore holds analytically. It naturally incorporates both variations in noise across pixels and correlations between neighboring pixels.

Evaluating Equation (B10) requires applying $\boldsymbol{\Sigma}^{-1}$ and computing $\ln(\det(\boldsymbol{\Sigma}))$. A straightforward Cholesky factorization $\boldsymbol{\Sigma} = \mathbf{L}\mathbf{L}^\top$ is $\mathcal{O}(N^3)$ per likelihood call (e.g., A. Krishnamoorthy & D. Menon 2011), which is too expensive to use inside nested sampling for every CCF realization. Instead of constructing $\boldsymbol{\Sigma}$ explicitly from the spectra, we approximate it at the CCF level with a simple AR(1) correlation model, which still captures the dominant neighboring-bin correlations while admitting an analytic, $\mathcal{O}(N)$ evaluation of the likelihood.

B.3. Practical Approach: AR(1) Likelihood Derivation

Starting from the full multivariate Gaussian likelihood (Equation (B10)), we derive an explicit closed-form expression for the likelihood under an AR(1) correlation model.

B.3.1. Covariance Structure

Let

$$e_i = y_i - m_i(\boldsymbol{\theta}) \tag{B12}$$

denote the residuals on the velocity grid $\{v_i\}_{i=1}^N$. We assume that the residuals follow a stationary AR(1) process:

$$e_i = \rho\, e_{i-1} + \varepsilon_i, \qquad |\rho| < 1, \tag{B13}$$

where ε_i is a zero-mean white-noise innovation with variance σ_ε^2. From the variance recursion, we obtain

$$\mathrm{Var}(e_i) = \sigma^2 = \frac{\sigma_\varepsilon^2}{1 - \rho^2}, \tag{B14}$$

and by induction on h, the lag–h correlation is

$$\mathrm{Corr}(e_i, e_{i+h}) = \rho^h. \tag{B15}$$

By iterating the AR(1) relation, we further obtain

$$\mathrm{Cov}(e_i, e_j) = \sigma^2 \rho^{|i-j|}. \tag{B16}$$

Allowing for heteroscedastic noise across the velocity grid, we define an approximate covariance matrix for the residual vector $\boldsymbol{e}$ as

$$\tilde{\boldsymbol{\Sigma}} = \boldsymbol{D}\boldsymbol{R}\boldsymbol{D} \approx \boldsymbol{\Sigma}, \tag{B17}$$

where $\boldsymbol{D} = \mathrm{diag}(\sigma_1, \ldots, \sigma_N)$, while $\sigma_i = \sqrt{\mathrm{Var}(e_i)}$ collects the per-bin standard deviations. The matrix $\boldsymbol{R}$ is the correlation matrix of the standardized residuals $z_i = e_i/\sigma_i$, whose elements are $R_{ij} = \rho^{|i-j|}$ and satisfy $\mathrm{Var}(z_i) = 1$.

B.3.2. Determinant of the Covariance Matrix

Using the multiplicative property of determinants, we have

$$\det(\tilde{\boldsymbol{\Sigma}}) = \det(\boldsymbol{D}\boldsymbol{R}\boldsymbol{D}) = \det(\boldsymbol{D})^2 \det(\boldsymbol{R}). \tag{B18}$$

Since $\det(\boldsymbol{D}) = \prod_{i=1}^N \sigma_i$, it follows that

$$\ln(\det(\tilde{\boldsymbol{\Sigma}})) = 2\sum_{i=1}^N \ln(\sigma_i) + \ln(\det(\boldsymbol{R})). \tag{B19}$$

B.3.3. Standardized Residuals

Defining the residual vector $\boldsymbol{z} = (z_1, \ldots, z_N)^\top$, the quadratic form becomes

$$(\boldsymbol{y} - \boldsymbol{m}(\boldsymbol{\theta}))^\top \tilde{\boldsymbol{\Sigma}}^{-1} (\boldsymbol{y} - \boldsymbol{m}(\boldsymbol{\theta})) = \boldsymbol{z}^\top \boldsymbol{R}^{-1} \boldsymbol{z}. \tag{B20}$$

B.3.4. Innovation Representation

For an AR(1) process, correlations between neighboring bins can be removed by an explicit lower-triangular linear transformation acting on the standardized residual vector. We define the lower-triangular matrix

$$\boldsymbol{J} = \begin{pmatrix} \sqrt{1-\rho^2} & 0 & 0 & \cdots & 0 \\ -\rho & 1 & 0 & \cdots & 0 \\ 0 & -\rho & 1 & \cdots & 0 \\ \vdots & \vdots & \vdots & \ddots & \vdots \\ 0 & 0 & 0 & -\rho & 1 \end{pmatrix}. \tag{B21}$$

Applying this transformation to the standardized residual vector $\boldsymbol{z}$ defines the innovation vector $\boldsymbol{\eta} = \boldsymbol{J}\boldsymbol{z}$, whose components are independent Gaussian variables with variance $(1-\rho^2)$. Explicitly

$$\eta_1 = \sqrt{1-\rho^2}\, z_1, \qquad \eta_i = z_i - \rho z_{i-1}, \quad i \geqslant 2. \tag{B22}$$

It follows that

$$\boldsymbol{R}^{-1} = (1-\rho^2)^{-1}\boldsymbol{J}^{\top}\boldsymbol{J}. \tag{B23}$$

Using this identity, the quadratic form in the likelihood can be written as

$$\boldsymbol{z}^{\top}\boldsymbol{R}^{-1}\boldsymbol{z} = (1-\rho^2)^{-1}\,\boldsymbol{z}^{\top}\boldsymbol{J}^{\top}\boldsymbol{J}\,\boldsymbol{z} = (1-\rho^2)^{-1}\,\boldsymbol{\eta}^{\top}\boldsymbol{\eta}. \tag{B24}$$

Since $\boldsymbol{\eta}^{\top}\boldsymbol{\eta} = \|\boldsymbol{\eta}\|_2^2$ is the squared Euclidean norm of the innovation vector, we obtain

$$\boldsymbol{\eta}^{\top}\boldsymbol{\eta} = \eta_1^2 + \sum_{i=2}^{N}\eta_i^2 = (1-\rho^2)z_1^2 + \sum_{i=2}^{N}(z_i - \rho z_{i-1})^2, \tag{B25}$$

and therefore

$$\boldsymbol{z}^{\top}\boldsymbol{R}^{-1}\boldsymbol{z} = z_1^2 + \frac{1}{1-\rho^2}\sum_{i=2}^{N}(z_i - \rho z_{i-1})^2. \tag{B26}$$

B.3.5. Determinant of the Correlation Matrix

From the triangular structure of $\boldsymbol{J}$, its determinant is given by the product of its diagonal elements:

$$\det(\boldsymbol{J}) = \sqrt{1-\rho^2}. \tag{B27}$$

Using Equation (B23) and the multiplicativity of the determinant, we obtain

$$\begin{aligned}\det(\boldsymbol{R}^{-1}) &= (1-\rho^2)^{-N}\det(\boldsymbol{J}^{\top})\det(\boldsymbol{J}) \\ &= (1-\rho^2)^{-N}\det(\boldsymbol{J})^2 = (1-\rho^2)^{-(N-1)}.\end{aligned} \tag{B28}$$

Taking the inverse gives

$$\det(\boldsymbol{R}) = (1-\rho^2)^{N-1}, \quad \ln(\det(\boldsymbol{R})) = (N-1)\ln(1-\rho^2). \tag{B29}$$

B.3.6. Final AR(1) Log Likelihood

Substituting the above expressions into the full likelihood yields

$$\boxed{\begin{aligned}\ln\mathcal{L}(\mathbf{y}|\boldsymbol{\theta},\,\rho) = &-\sum_{i=1}^{N}\ln\sigma_i - \frac{N-1}{2}\ln(1-\rho^2) \\ &-\frac{1}{2}\left[z_1^2 + \frac{1}{1-\rho^2}\sum_{i=2}^{N}(z_i - \rho z_{i-1})^2\right] - \frac{N}{2}\ln(2\pi).\end{aligned}} \tag{B30}$$

This expression is exact for the AR(1) covariance model and can be evaluated in $\mathcal{O}(N)$ time without explicitly constructing or inverting the covariance matrix.

B.4. Implementation Details and Estimation of the AR(1) Coefficient

In the implementation used for the Bayesian model comparison, the constant term $-(N/2)\ln(2\pi)$ in the log likelihood is dropped, as it cancels in Bayes factors and does not affect posterior inferences.

B.4.1. Estimating the Per-bin Scatter

The standard deviations σ_i at each velocity bin are estimated empirically from the Monte Carlo ensemble of CCF realizations for a fixed planet, exposure time, and molecule. To avoid letting localized structures in the planetary and telluric regions dominate the noise estimate, we replace σ_i within $|v - v_{\rm tot}| \leqslant 40\,{\rm km\,s^{-1}}$ and $|v| \leqslant 40\,{\rm km\,s^{-1}}$ by the median standard deviation measured outside these intervals. Elsewhere, the full velocity dependence of σ_i is retained.

B.4.2. Estimating the Correlation Parameter

The correlation parameter ρ is estimated using the same off-peak velocity regions defined above, i.e., excluding $\pm 40\,{\rm km\,s^{-1}}$ around $v_{\rm tot}$ and zero velocity, so that neither planetary signal nor telluric residuals contribute to the estimator. From the $N_{\rm off}$ off-peak velocity bins, we form

$$u_k = y_{i_k} - \mathrm{median}\Big(\{y_{i_k}\}_{k=1}^{N_{\rm off}}\Big), \tag{B31}$$

where $\{i_k\}_{k=1}^{N_{\rm off}}$ are the indices of the retained off-peak velocity bins in the full CCF grid. To limit the influence of outliers, we compute the median absolute deviation (MAD) of $\{u_k\}_{k=1}^{N_{\rm off}}$ and winsorize the sequence at ± 3MAD:

$$u_k^{(w)} = \mathrm{clip}(u_k,\ -3\mathrm{MAD},\ 3\mathrm{MAD}). \tag{B32}$$

The lag-1 correlation coefficient is estimated using the Yule–Walker estimator for an AR(1) process (G. U. Yule 1927; G. Walker 1931; P. J. Brockwell & R. A. Davis 1991):

$$\gamma(1) = \mathrm{Cov}(u_k^{(w)}, u_{k-1}^{(w)}) = \rho\,\gamma(0), \quad \gamma(0) = \mathrm{Var}(u_k^{(w)}), \tag{B33}$$

implying

$$\rho = \frac{\gamma(1)}{\gamma(0)} = \frac{\mathrm{Cov}(u_k^{(w)}, u_{k-1}^{(w)})}{\mathrm{Var}(u_k^{(w)})}. \tag{B34}$$

Replacing the population moments by their empirical counterparts:

$$\hat{\gamma}(1) = \frac{1}{N_{\rm off} - 1} \sum_{k=2}^{N_{\rm off}} u_k^{(w)}\, u_{k-1}^{(w)}, \quad \hat{\gamma}(0) = \frac{1}{N_{\rm off}} \sum_{k=1}^{N_{\rm off}} \left(u_k^{(w)}\right)^2, \tag{B35}$$

yields the practical Yule–Walker estimator

$$\boxed{\hat{\rho}_{\rm w} = \frac{\hat{\gamma}(1)}{\hat{\gamma}(0)} = \frac{N_{\rm off}}{N_{\rm off} - 1} \frac{\sum_{k=2}^{N_{\rm off}} u_k^{(w)}\, u_{k-1}^{(w)}}{\sum_{k=1}^{N_{\rm off}} \left(u_k^{(w)}\right)^2}.} \tag{B36}$$

B.4.3. Final Likelihood Evaluation

For a given planet, exposure time, and molecule, the estimated $\hat{\rho}_{\rm w}$ is treated as fixed and is not sampled as a free parameter. The covariance matrix is constructed as $\tilde{\boldsymbol{\Sigma}} = \boldsymbol{D}\boldsymbol{R}(\hat{\rho}_{\rm w})\boldsymbol{D}$, and the AR(1) log likelihood derived in Section B.3.6 is evaluated for each CCF realization. This approach accounts explicitly for velocity-bin correlations, reduces the effective number of independent samples when $\hat{\rho}_{\rm w} > 0$, and yields deliberately conservative Bayes factors, while avoiding the computational cost of full pixel-space covariance treatments.

Appendix C
Monte Carlo Stability and Stopping Criterion

To quantify the Monte Carlo uncertainty in the final Bayes factors, we run the pipeline M times per configuration. Here, we assess whether $M = 100$ is sufficiently precise for our purposes.

We estimate the standard error (SE) of the sample median and its associated margin of error (MoE) at 95% confidence. Let s denote the Monte Carlo standard deviation, i.e., the between-realization scatter of the detection statistic. As a working approximation, when the underlying distribution is close to normal, the SE of the sample median is

$$\mathrm{SE} \approx 1.253\, \frac{s}{\sqrt{M}}, \tag{C1}$$

which is the standard asymptotic normal-approximation result for the variance of the sample median (e.g., C. Walck 1996). For a two-sided 95% confidence interval, we then define

$$\mathrm{MoE}_{95} = 1.96\mathrm{SE}. \tag{C2}$$

For each configuration, we compute MoE_{95} and define a relative, scale-aware metric:

$$\mathrm{rMoE}_{95} = \frac{\mathrm{MoE}_{95}}{\max(|\tilde{x}|,\, 0.5)}, \tag{C3}$$

where $\tilde{x}$ is the sample median of $\log_{10} B$. We adopt the following stopping criterion: if $\mathrm{rMoE}_{95} < 0.5$, the median $\log_{10} B$ is considered sufficiently precise for assigning a Jeffreys category; otherwise, we increase M and recompute until the condition is satisfied. The threshold $\mathrm{rMoE}_{95} < 0.5$ is an operational choice adopted in this work.

This definition scales the 95% MoE for $\tilde{x}$ either to the signal amplitude itself (for large $|\tilde{x}|$) or to one Jeffreys step (0.5) when $|\tilde{x}|$ is small. As a result, strong signals are not overpenalized, while weak signals do not render Equation (C3) unstable near zero. This helps ensure that Jeffreys-category assignments are not driven by Monte Carlo noise.

Since $\mathrm{MoE}_{95} \propto M^{-1/2}$ for fixed variance, rMoE_{95} decreases on average with the number of realizations M. In practice, the procedure reaches the target precision after a finite number of realizations for the cases considered here, as illustrated in Figure C1.

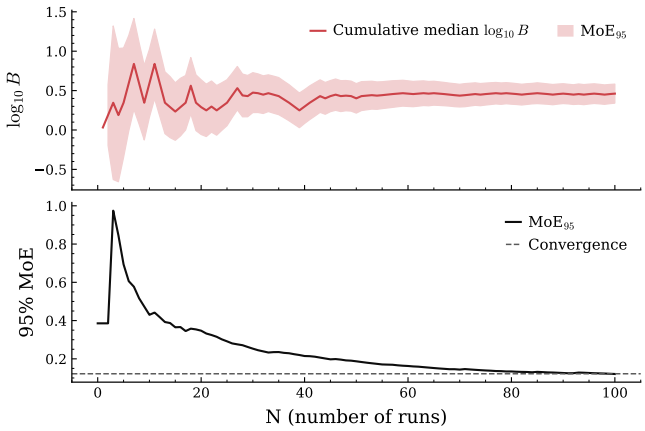


Figure C1. Results from $M = 100$ independent simulation realizations followed by Bayesian analysis, shown for H_2O, on LP 890-9 c, after 20 transits. Top: the cumulative median of $\log_{10} B$ stabilizes by $M \approx 80$ realizations while the 95% confidence interval narrows. Bottom: the 95% MoE on $\log_{10} B$ decreases approximately as $M^{-1/2}$ and stabilizes by $M \approx 90$. At that point the convergence criterion is met, yielding a statistically stable estimate of $\log_{10} B$.

Appendix D
Band-limited Mode and Comparisons

While no published study appears to provide an equally detailed ANDES-specific analysis for potentially habitable rocky exoplanets, several works have investigated this topic using general parameters representative of a high-resolution spectrograph on an extremely large telescope (e.g., Y. Fujii et al. 2018; M. H. Currie et al. 2023). In our analysis, we obtain one CCF per realization and exposure setting over the full wavelength range of ANDES. This approach is appropriate because ANDES will use its entire spectral range simultaneously.[15] However, a full-range detection metric is only directly comparable to the initial forward-model detectability forecasts of E. Palle et al. (2025; see Section 8.2), whereas most previous studies assess detectability within individual molecular bands (e.g., F. Wunderlich et al. 2020; M. H. Currie et al. 2023). We therefore consider, in addition to the full-wavelength-range analysis, a band-limited mode that applies the same masking and processing steps but restricts the cross correlation to spectral intervals corresponding to relevant molecular bands. This allows us to evaluate molecule-specific spectral windows independently, even though ANDES can in principle be used over the full wavelength range simultaneously.

In light of the extensive literature on the TRAPPIST-1 system, we use this band-limited mode and compile Table D1, which reports the number of transits required to reach a detection threshold of $\log_{10} B = 5.43$ for various bands on TRAPPIST-1 e. Values are reported at 20, 50, 100, 200, 250, and 300 transits using the interpolation in Section 7, and the

[15] https://elt.eso.org/instrument/ANDES/

Table D1
Transit Requirements for Detecting Different Molecular Bands on TRAPPIST-1 e

Band (μm)	Transits Required (This Work) ($\log_{10}B = 5.43$)	M. H. Currie et al. (2023) (5σ)	F. Wunderlich et al. (2020) (5σ)
CO_2; 1.56–1.62	151	34	⋯
O_2; 1.24–1.30	>300	200	910
CH_4; 1.62–1.70	>300	33	⋯
H_2O; 0.90–0.98	>300	>300	⋯

Note. Number of transits required to reach a band detection threshold of $\log_{10}B = 5.43$ (used here only as a rough comparability proxy to "5σ" studies; see Appendix D). Values are reported for each relevant spectral band from our band-limited mode, with additional columns comparing to estimates from M. H. Currie et al. (2023) and F. Wunderlich et al. (2020). As discussed in Appendix D, such σ-based comparisons should be treated with caution; we interpret results via Bayes factors, whereas the cited works adopt frequentist significance.

table contains comparisons to previous studies. The specific threshold of $\log_{10}B = 5.43$ corresponds, via the heuristic relation $n_\sigma \approx \sqrt{2\ln B}$ as written by D. Kipping & B. Benneke (2025) and motivated by the asymptotic connection between Bayes factors and likelihood-ratio statistics discussed by R. E. Kass & A. E. Raftery (1995), to roughly 5σ. We adopt this only as a heuristic reference to facilitate comparison with earlier work that reported results in σ units. We stress that such conversions between Bayes factors and frequentist significance are not formally defined and should not be interpreted literally, as discussed by D. Kipping & B. Benneke (2025) and D. P. Thorngren et al. (2026). Our analysis itself is expressed entirely in terms of Bayes factors. For interpretation, readers should rely on the Bayes factors themselves; the σ proxy is provided solely for approximate comparability.

This comparison also illustrates the impact of wavelength coverage on transit requirements. A limited spectral range such as the H band can contain much of the information for some species, especially CO_2 near 1.6 μm, but it does not provide an equally effective basis for all molecules. CH_4 and H_2O draw important information from multiple NIR regions, including longer wavelengths, while O_2 relies on bands at shorter wavelengths and remains strongly affected by telluric overlap. Therefore, the advantage of broad simultaneous wavelength coverage is not that every wavelength contributes equally, but that different molecules draw their detectability from different parts of the optical–NIR range. In the ETC setup adopted in this work, however, the retained seeing-limited wavelength range does not include the K band, which is particularly relevant for molecules with strong longer-wavelength NIR bands, such as CH_4 and H_2O.

ORCID iDs

Evann Kurzawa-Ferrandez https://orcid.org/0009-0006-1858-8166
Aaron Bello-Arufe https://orcid.org/0000-0003-3355-1223
Renyu Hu https://orcid.org/0000-0003-2215-8485

References

Abdurro'uf, Accetta, K., Aerts, C., et al. 2022, ApJS, 259, 35
Agol, E., Dorn, C., Grimm, S. L., et al. 2021, PSJ, 2, 1
Allard, F., & Hauschildt, P. H. 1995, ApJ, 445, 433
Allen, N. H., Espinoza, N., Diamond-Lowe, H., et al. 2025, AJ, 170, 240
Astropy Collaboration 2022, ApJ, 935, 167
August, P. C., Buchhave, L. A., Diamond-Lowe, H., et al. 2025, A&A, 695, A171
Bainbridge, A. E., & Heidt, L. E. 1966, Tell, 18, 221
Barber, R. J., Tennyson, J., Harris, G. J., & Tolchenov, R. N. 2006, MNRAS, 368, 1087
Bekki, S., & Lefevre, F. 2009, EPJWC, 1, 113
Bello-Arufe, A., Cabot, S. H. C., Mendonça, J. M., Buchhave, L. A., & Rathcke, A. D. 2022, AJ, 163, 96
Bello-Arufe, A., Damiano, M., Bennett, K. A., et al. 2025, ApJL, 980, L26
Bello-Arufe, A., Knutson, H. A., Mendonça, J. M., et al. 2023, AJ, 166, 69
Berger, T. A., Huber, D., Gaidos, E., & van Saders, J. L. 2018, ApJ, 866, 99
Bertaux, J. L., Lallement, R., Ferron, S., Boonne, C., & Bodichon, R. 2014, A&A, 564, A46
Bétrémieux, Y., & Kaltenegger, L. 2013, ApJL, 772, L31
Bishop, C. M. 2006, Pattern Recognition and Machine Learning, Information Science and Statistics (Springer)
Bohl, A., Lawrence, L., Lowry, G., & Kaltenegger, L. 2026, MNRAS, 547, stag028
Bonomo, A. S., Dumusque, X., Massa, A., et al. 2023, A&A, 677, A33
Borucki, W., Thompson, S. E., Agol, E., & Hedges, C. 2018, NewAR, 83, 28
Borucki, W. J., Agol, E., Fressin, F., et al. 2013, Sci, 340, 587
Brockwell, P. J., & Davis, R. A. 1991, Time Series: Theory and methods (Springer)
Brogi, M., Line, M., Bean, J., Désert, J. M., & Schwarz, H. 2017, ApJL, 839, L2
Brogi, M., & Line, M. R. 2019, AJ, 157, 114
Brogi, M., Snellen, I. A. G., de Kok, R. J., et al. 2013, ApJ, 767, 27
Buchner, J. 2016, PyMultiNest: Python interface for MultiNest, Astrophysics Source Code Library, ascl:1606.005
Cadieux, C., Doyon, R., MacDonald, R. J., et al. 2024b, ApJL, 970, L2
Cadieux, C., Plotnykov, M., Doyon, R., et al. 2024a, ApJL, 960, L3
Cauley, P. W., Kuckein, C., Redfield, S., et al. 2018, AJ, 156, 189
Christiansen, J. L., McElroy, D. L., Harbut, M., et al. 2025, PSJ, 6, 186
Crossfield, I. J. M., Ciardi, D. R., Petigura, E. A., et al. 2016, ApJS, 226, 7
Currie, M. H., Meadows, V. S., & Rasmussen, K. C. 2023, PSJ, 4, 83
Cutri, R., Skrutskie, M., Dyk, S., et al. 2003, yCat 2246, 0
Czesla, S., Schröter, S., Schneider, C. P., et al. 2019, PyA: Python astronomy-related packages, Astrophysics Source Code Library, ascl:1906.010
Damiano, M., Bello-Arufe, A., Yang, J., & Hu, R. 2024, ApJL, 968, L22
de Kok, R. J., Brogi, M., Snellen, I. A. G., et al. 2013, A&A, 554, A82
Delrez, L., Murray, C. A., Pozuelos, F. J., et al. 2022, A&A, 667, A59
Diamond-Lowe, H., Kreidberg, L., Harman, C. E., et al. 2022, AJ, 164, 172
D'Odorico, V., Bolton, J. S., Christensen, L., et al. 2024, ExA, 58, 21
Dransfield, G., Timmermans, M., Triaud, A. H. M. J., et al. 2024, MNRAS, 527, 35
Dressing, C. D., Vanderburg, A., Schlieder, J. E., et al. 2017, AJ, 154, 207
Edlén, B. 1966, Metro, 2, 71
El Amraoui, L., Attié, J.-L., Ricaud, P., et al. 2014, AMT, 7, 3035
Espinoza, N., Allen, N. H., Glidden, A., et al. 2025, ApJL, 990, L52
Feroz, F., Hobson, M. P., & Bridges, M. 2009, MNRAS, 398, 1601
Fortune, M., Gibson, N. P., Diamond-Lowe, H., et al. 2025, A&A, 701, A25
Fujii, Y., Angerhausen, D., Deitrick, R., et al. 2018, AsBio, 18, 739
Fukui, A., Livingston, J., Narita, N., et al. 2016, AJ, 152, 171
Fulton, B. J., Petigura, E. A., Howard, A. W., et al. 2017, AJ, 154, 109
Gaia Collaboration 2023, A&A, 674, A1
Gajdoš, P., Vaňko, M., & Parimucha, Š. 2019, RAA, 19, 041
Gandhi, S., Brogi, M., & Webb, R. K. 2020, MNRAS, 498, 194
Gentine, P., Holtslag, A. A. M., D'Andrea, F., & Ek, M. 2013, JHyMe, 14, 1443
Gibson, N. P., Merritt, S., Nugroho, S. K., et al. 2020, MNRAS, 493, 2215
Gilbert, E. A., Vanderburg, A., Rodriguez, J. E., et al. 2023, ApJL, 944, L35
Gillon, M., Ducrot, E., Bell, T. J., et al. 2026, NatAs, 10, 674
Gizis, J. E., Monet, D. G., Reid, I. N., et al. 2000, AJ, 120, 1085
Glidden, A., Ranjan, S., Seager, S., et al. 2025, ApJL, 990, L53
Gordon, I. E., Rothman, L. S., Hargreaves, R. J., et al. 2022, JQSRT, 277, 107949
Gressier, A., Espinoza, N., Allen, N. H., et al. 2024, ApJL, 975, L10
Grimm, S. L., & Heng, K. 2015, ApJ, 808, 182
Grimm, S. L., Malik, M., Kitzmann, D., et al. 2021, ApJS, 253, 30
Hamilton, J. D. 1994, Time Series Analysis (Princeton Univ. Press)
Hardegree-Ullman, K. K., Apai, D., Bergsten, G. J., Pascucci, I., & López-Morales, M. 2023, AJ, 165, 267
Hardegree-Ullman, K. K., Apai, D., Haffert, S. Y., et al. 2025, AJ, 169, 171

Hardegree-Ullman, K. K., Cushing, M. C., Muirhead, P. S., & Christiansen, J. L. 2019, AJ, 158, 75
Hargreaves, R. J., Gordon, I. E., Rey, M., et al. 2020, ApJS, 247, 55
Heise, S., Wickert, J., Beyerle, G., Schmidt, T., & Reigber, C. 2006, AdSpR, 37, 2222
Hill, M. L., Bott, K., Dalba, P. A., et al. 2023, AJ, 165, 34
Jenkins, J. M., Twicken, J. D., Batalha, N. M., et al. 2015, AJ, 150, 56
Jönsson, H., Holtzman, J. A., Allende Prieto, C., et al. 2020, AJ, 160, 120
Kanodia, S., & Wright, J. 2018, RNAAS, 2, 4
Kasper, D., Bean, J. L., Line, M. R., et al. 2023, AJ, 165, 7
Kass, R. E., & Raftery, A. E. 1995, JASA, 90, 773
Kasting, J. F., Whitmire, D. P., & Reynolds, R. T. 1993, Icar, 101, 108
Kausch, W., Noll, S., Smette, A., et al. 2015, A&A, 576, A78
Kawahara, H., Matsuo, T., Takami, M., et al. 2012, ApJ, 758, 13
Kiehl, J. T., & Yamanouchi, T. 1985, TellB, 37, 1
Kipping, D., & Benneke, B. 2025, arXiv:2506.05392
Kjærsgaard, R. D., Bello-Arufe, A., Rathcke, A. D., Buchhave, L. A., & Clemmensen, L. K. H. 2023, A&A, 677, A120
Kopparapu, R. K., Ramirez, R., Kasting, J. F., et al. 2013, ApJ, 765, 131
Krishnamoorthy, A., & Menon, D. 2011, arXiv:1111.4144
Kuttippurath, J., Pillai Gopikrishnan, G., Müller, R., Godin-Beekmann, S., & Brioude, J. 2024, ACP, 24, 6743
Lan, X., Thoning, K., & Dlugokencky, E. 2025, Trends in globally-averaged CH4, N2O, and SF6 determined from NOAA Global Monitoring Laboratory measurements, v2025-09, https://gml.noaa.gov/ccgg/trends/
López-Morales, M., Ben-Ami, S., Gonzalez-Abad, G., et al. 2019, AJ, 158, 24
Luque, R., Coy, B. P., Xue, Q., et al. 2025, AJ, 170, 49
Lustig-Yaeger, J., Meadows, V. S., & Lincowski, A. P. 2019, AJ, 158, 27
Maiolino, R., Haehnelt, M., Murphy, M. T., et al. 2013, arXiv:1310.3163
Marconi, A., Abreu, M., Adibekyan, V., et al. 2022, SPIE, 12184, 1218424
Marconi, A., Abreu, M., Adibekyan, V., et al. 2024, SPIE, 13096, 1309613
Martin, P. E., & Barker, E. F. 1932, PhRv, 41, 291
Martins, C. J. A. P., Cooke, R., Liske, J., et al. 2024, ExA, 57, 5
Mawet, D., Ruane, G., Xuan, W., et al. 2017, ApJ, 838, 92
Mazeh, T., Tamuz, O., & Zucker, S. 2007, ASPC, 366, 119
Meadows, V. S., Reinhard, C. T., Arney, G. N., et al. 2018, AsBio, 18, 630
Meech, A., Aigrain, S., Brogi, M., & Birkby, J. L. 2022, MNRAS, 512, 2604
Meier Valdés, E. A., Demory, B. O., Diamond-Lowe, H., et al. 2025, A&A, 698, A68
Mollière, P., Wardenier, J. P., van Boekel, R., et al. 2019, A&A, 627, A67
Morley, C. V., Kreidberg, L., Rustamkulov, Z., Robinson, T., & Fortney, J. J. 2017, ApJ, 850, 121
Morton, T. D., Bryson, S. T., Coughlin, J. L., et al. 2016, ApJ, 822, 86
Prather, M. J. 1989, in An Assessment Model for Atmospheric Composition (NASA) https://ntrs.nasa.gov/api/citations/19890011217/downloads/19890011217.pdf
Oman, L., Waugh, D. W., Pawson, S., Stolarski, R. S., & Nielsen, J. E. 2008, JAtS, 65, 3278
Palle, E., Biazzo, K., Bolmont, E., et al. 2025, ExA, 59, 29
Pan, L. L., Randel, W. J., Gary, B. L., Mahoney, M. J., & Hintsa, E. J. 2004, JGRD, 109, D23103
Parmentier, V., & Guillot, T. 2014, A&A, 562, A133
Parviainen, H., Luque, R., & Palle, E. 2024, MNRAS, 527, 5693
PHL @ UPR Arecibo 2026, Habitable Worlds Catalog, http://phl.upr.edu/hwc
Piaulet-Ghorayeb, C., Benneke, B., Turbet, M., et al. 2025, ApJ, 989, 181
Pickles, A. J. 1998, PASP, 110, 863
Pidhorodetska, D., Fauchez, T. J., Villanueva, G. L., Domagal-Goldman, S. D., & Kopparapu, R. K. 2020, ApJL, 898, L33
Pierrehumbert, R. T. 2010, Principles of Planetary Climate (Cambridge Univ. Press)
Piskunov, N., Rains, A. D., & Boldt-Christmas, L. 2025, arXiv, arXiv:2509.12737
Pueyo, L., Stark, C., Juanola-Parramon, R., et al. 2019, SPIE, 11117, 1111703
Quintana, E. V., Barclay, T., Raymond, S. N., et al. 2014, Sci, 344, 277
Rackham, B. V., Apai, D., & Giampapa, M. S. 2018, ApJ, 853, 122
Ramirez, R. M. 2018, Geosc, 8, 280
Rathcke, A. D., Buchhave, L. A., de Wit, J., et al. 2025, ApJL, 979, L19
Robinson, T. D., & Catling, D. C. 2012, ApJ, 757, 104
Robinson, T. D., & Catling, D. C. 2014, NatGe, 7, 12
Robinson, T. D., Fortney, J. J., & Hubbard, W. B. 2017, ApJ, 850, 128
Rodler, F., & López-Morales, M. 2014, ApJ, 781, 54
Roederer, I. U., Alvarado-Gómez, J. D., Allende Prieto, C., et al. 2024, ExA, 57, 17
Rothman, L. S., Gordon, I. E., Barber, R. J., et al. 2010, JQSRT, 111, 2139
Rothman, L. S., Gordon, I. E., Babikov, Y., et al. 2013, JQSRT, 130, 4
Rukdee, S. 2024, NatSR, 14, 27356
Said, A., Davizón, Y. A., Espino-Román, P., Rodríguez-Said, R., & Hernández-Santos, C. 2016, Symm, 8, 78
Sanna, N., Oliva, E., Massi, F., Cresci, G., & Origlia, L. 2014, SPIE, 9147, 914790
Sanna, N., Oliva, E., & Origlia, L. 2021, The Exposure Time Calculator for HIRES@ELT, O.A. Arcetri 74, INAF http://hdl.handle.net/20.500.12386/30532
Sanna, N., Canto Martins, B. L., Martins, A. M., et al. 2024, SPIE, 13096, 130964G
Schwieterman, E. W., Kiang, N. Y., Parenteau, M. N., et al. 2018, AsBio, 18, 663
Seager, S., & Sasselov, D. D. 2000, ApJ, 537, 916
Seager, S., Schrenk, M., & Bains, W. 2012, AsBio, 12, 61
Serindag, D. B., & Snellen, I. A. G. 2019, ApJL, 871, L7
Siffert, B. B., Gonçalves Farias, R. G., Garcia, M., et al. 2024, MNRAS, 530, 4331
Smette, A., Sana, H., Noll, S., et al. 2015, A&A, 576, A77
Smith, P. C. B., Line, M. R., Bean, J. L., et al. 2024, AJ, 167, 110
Snellen, I., de Kok, R., Birkby, J. L., et al. 2015, A&A, 576, A59
Snellen, I. A. G., de Kok, R. J., le Poole, R., Brogi, M., & Birkby, J. 2013, ApJ, 764, 182
Stassun, K. G., Oelkers, R. J., Paegert, M., et al. 2019, AJ, 158, 138
Suissa, G., Wolf, E. T., Kopparapu, R., et al. 2020, AJ, 160, 118
Tamuz, O., Mazeh, T., & Zucker, S. 2005, MNRAS, 356, 1466
Tennyson, J., Bernath, P. F., Brown, L. R., et al. 2013, JQSRT, 117, 29
Thompson, M. A., Krissansen-Totton, J., Wogan, N., Telus, M., & Fortney, J. J. 2022, PNAS, 119, e2117933119
Thorngren, D. P., Sing, D. K., & Mukherjee, S. 2026, ApJS, 283, 10
Torres, G., Kipping, D. M., Fressin, F., et al. 2015, ApJ, 800, 99
Vanderburg, A., Rowden, P., Bryson, S., et al. 2020, ApJL, 893, L27
Vaughan, S. R., Birkby, J. L., Thatte, N., et al. 2024, MNRAS, 528, 3509
Vergados, P., Mannucci, A. J., Ao, C. O., Verkhoglyadova, O., & Iijima, B. 2018, AMT, 11, 1193
Virtanen, P., Gommers, R., Oliphant, T. E., et al. 2020, NatMe, 17, 261
von Paris, P., Cabrera, J., Godolt, M., et al. 2011, A&A, 534, A26
von Paris, P., Hedelt, P., Selsis, F., Schreier, F., & Trautmann, T. 2013, A&A, 551, A120
Walck, C. 1996, Hand-book on Statistical Distributions for Experimentalists (Stockholms Universitet) https://api.semanticscholar.org/CorpusID:122813337
Walker, G. 1931, RSPSA, 131, 518
Wang, J., Mawet, D., Hu, R., et al. 2018, JATIS, 4, 035001
Wang, J., Mawet, D., Ruane, G., Hu, R., & Benneke, B. 2017, AJ, 153, 183
Wang, J. J., Delorme, J.-R., Ruffio, J.-B., et al. 2021, SPIE, 11823, 1182302
Weiss, L. M., Isaacson, H., Howard, A. W., et al. 2024, ApJS, 270, 8
Western, C. M., Carter-Blatchford, L., Crozet, P., et al. 2018, JQSRT, 219, 127
Wilks, D. S. 2011, Statistical Methods in the Atmospheric Sciences (Elsevier)
Wright, J. T., & Eastman, J. D. 2014, PASP, 126, 838
Wunderlich, F., Scheucher, M., Godolt, M., et al. 2020, ApJ, 901, 126
Yang, J., Cowan, N. B., & Abbot, D. S. 2013, ApJL, 771, L45
Yule, G. U. 1927, RSPTA, 226, 267
Yurchenko, S. N., Owens, A., Kefala, K., & Tennyson, J. 2024, MNRAS, 528, 3719
Yurchenko, S. N., & Tennyson, J. 2014, MNRAS, 440, 1649
Zhang, H., Wang, J., & Plummer, M. K. 2024, AJ, 167, 37